Late Miocene seasonal to subdecadal climate variability in the Indo-West Pacific (East Kalimantan, Indonesia) preserved in giant clams

V. Warter, W. Müller, F.P. Wesselingh (Frank), J. Todd, W. Renema (Willem)

PALAIOS
Emphasizing the impact of life on Earth's history

PALAIOS, 2015, v. 30, 66–82
Research Article
DOI: http://dx.doi.org/10.2110/palo.2013.061

LATE MIOCENE SEASONAL TO SUBDECADAL CLIMATE VARIABILITY IN THE INDO-WEST PACIFIC (EAST KALIMANTAN, INDONESIA) PRESERVED IN GIANT CLAMS

VIOLA WARTER,[1] WOLFGANG MÜLLER,[1] FRANK P. WESSELINGH,[2] JONATHAN A. TODD,[3] AND WILLEM RENEMA[2]
[1]*Royal Holloway University of London, Department of Earth Sciences, Egham, Surrey, TW20 0EX, U.K.*
[2]*Naturalis Biodiversity Center, Department of Geology, P.O. Box 9517, Leiden, 2300 RA, The Netherlands*
[3]*Natural History Museum, Department of Earth Sciences, Cromwell Road, London, SW7 5BD, U.K.*
e-mail: viola.warter@rhul.ac.uk

ABSTRACT: **Two late Miocene *Tridacna* (giant clam) shells from East Kalimantan (Indonesia) were investigated in order to evaluate their potential as subannually resolved paleoenvironmental archives. Via a combination of X-ray diffraction (XRD), laser ablation–inductively coupled plasma–mass spectrometry (LA-ICPMS) trace element analysis, scanning electron microscopy (SEM) and cathodoluminescence (CL) imaging, pristine versus diagenetically altered domains within the shells were identified. LA-ICPMS transects targeting altered aragonite and calcite zones reveal distinct compositional differences in elemental ratios (B/Ca, Mg/Ca, Sr/Ca/ Ba/Ca, Mn/Ca, Al/Ca, La/Ca, Ce/Ca) relative to primary shell aragonite. Pristine shell domains are characterized by an intact banding pattern of alternating dark and light growth bands, with which spatially resolved LA-ICPMS element/Ca and micromilled $\delta^{18}O$ records were aligned. Light $\delta^{18}O$ values correspond to dark growth bands, indicating growth during warm seasons. The Mg/Ca and/or Sr/Ca ratios covary with oscillating stable oxygen isotope profiles. Progressive increase in Mg/Ca with age demonstrates that besides temperature, growth kinetics exert control over Mg incorporation. If interpreted as temperature controlled only, $\delta^{18}O$ from both shells represents average seasonal sea-surface temperature (SST) variability of 2.7 ± 2.1 and 4.6 ± 1.7 °C, respectively. Using published temperature equations and assuming $\delta^{18}O_{sw} = -0.88‰$, corresponding mean annual paleo–sea-surface temperatures of 27.8 ± 0.2 and 28.5 ± 0.2 °C are estimated. Although the fossil *Tridacna* shells were noticeably affected by alteration on their external surfaces, their internal aragonitic structure is, to a large extent, well preserved. These corresponding paleoproxy records provide detailed insight into tropical SST variability of the Indo-Pacific region during the late Miocene.**

INTRODUCTION

The Miocene is an epoch of major change with respect to the Cenozoic climate history (Flower and Kennett 1994). While the overall Miocene climatic evolution is well documented by the stable isotope record derived from oceanic benthic foraminifera tests (Lear et al. 2000; Zachos et al. 2001 2008; Billups and Schrag 2003), the mechanisms causing Miocene climate change are not well understood (Holbourn et al. 2007; Herold et al. 2012).

The Indonesian Throughflow (ITF), a system of currents, surface, and thermocline waters, passes through today's last remaining low-latitude ocean passage, the SE Asian gateway, which connects the Pacific and Indian oceans. It is considered to be a key initiator of climate change during the Miocene and Pliocene, not only for the Southeast Asian region but also on a global scale (Cane and Molnar 2001; Kuhnt et al. 2004; Singh and Gupta 2010). The modern ITF intensity exhibits a significant interannual variability, which is closely linked to the geographic extent and position of the West Pacific Warm Pool (Kuhnt et al. 2004) and El Niño–Southern Oscillation (ENSO) patterns (England and Huang 2005). The paleoceanographic history of the Indonesian Gateway and associated long-term fluctuations in water mass throughflow are strongly controlled by the tectonic reorganization caused by convergence of the Indo-Australian and Philippine-Pacific plates with the stable Asian craton (Hall et al. 2011). Collision between the Australian plate and the island arcs on the Pacific plates initiated in the earliest Miocene (Srinivasan and Sinha 2000; Kuhnt et al. 2004; Hall et al. 2011). The interaction between the complex tectonic history of the Southeast Asia–Australia collision zone, corresponding oceanographic modulations of the Indonesian Gateway, the associated climate and environmental change, and the resulting biotic response during the Miocene are not well understood, even though they must have interplayed (Renema et al. 2008).

Very few paleoclimate proxy records (especially from pre-Quaternary time) from the ITF area exist that give insight into its tectonic and paleocenographic evolution (Kuhnt et al. 2004). However, such records are essential to quantify paleoclimate dynamics and to disentangle their causes and effects. Furthermore, existing paleoclimate proxy data are mostly derived from the open marine and/or high-latitude realm, while direct evidence of paleoclimate from shallow water in low latitudes is rare.

Highly time-resolved paleoclimate records are of special interest, because they allow the assessment of seasonal to interannual sea-surface temperature (SST) variability, like ENSO- or monsoon-related changes in SST. Changes in seasonality play an important role with respect to (abrupt) climate changes (Crowley et al. 1986; Denton et al. 2005; Ayling et al. 2006; Fluckiger et al. 2008). Hence, SST variations (even if recorded over a relatively short period only) might contribute to our understanding of long-term climate change.

Foraminiferan records have traditionally been used to reconstruct paleotemperature/ice volume over the last ~65 myr (Zachos et al. 2001 2008). However, individuals are usually too short-lived to reflect seasonal variability. Coral skeletons are frequently used as paleoenvironmental archives for reconstructions for Pleistocene or younger strata (Alibert and

Published Online: February 2015
 0883-1351/15/030-066/$03.00

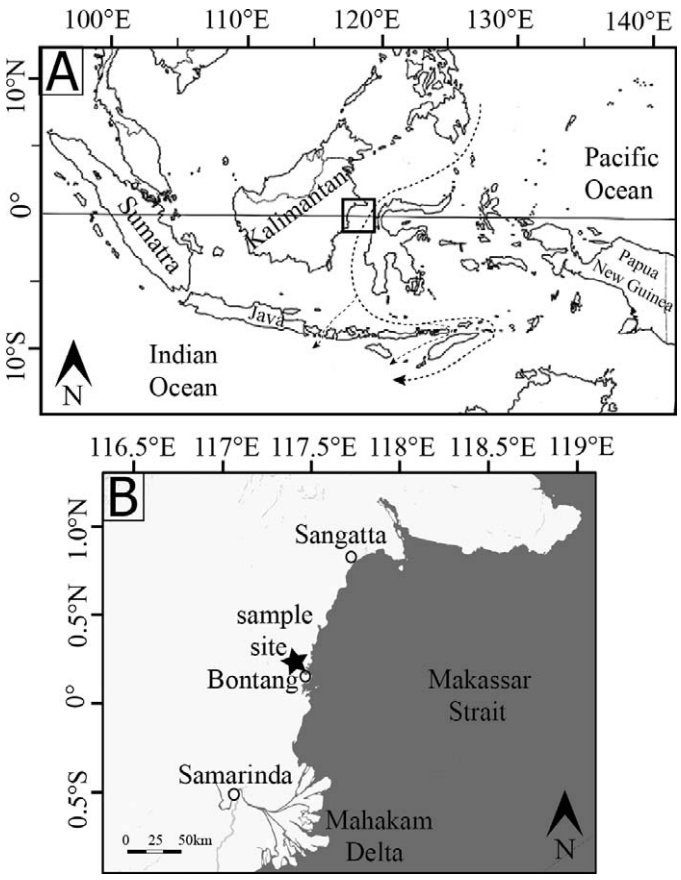

FIG. 1.—Location of study area. **A)** Overview map of the Indo-Pacific study area including the main Throughflow passages (marked by dashed arrows). **B)** Coast of East Kalimantan including Bontang and the nearby sample site with outcrops TF108 and TF109 (marked by star).

McCulloch 1997; Gagan et al. 2000; Quinn and Sampson 2002; Swart et al. 2002; Corrège et al. 2004; Mishima et al. 2009). Coral-based proxies from the Miocene, however, are still rare (Mertz-Kraus et al. 2009; Griffiths et al. 2013). Due to their porous structure and metastable aragonite mineralogy, coral skeletons are highly susceptible to diagenetic processes that affect the original shell geochemistry and challenge their reliability as environmental recorders (McGregor and Gagan 2003; Allison et al. 2007; Hendy et al. 2007; Nothdurft and Webb 2009; Hathorne et al. 2011; Sayani et al. 2011; Griffiths et al. 2013).

Bivalves build a dense shell structure, which makes the shells less prone to diagenetic alteration and thus enhances their preservation potential. Due to their outstanding longevity of up to several decades (Watanabe et al. 2004), giant clams (family Cardiidae, subfamily Tridacninae, genus *Tridacna*) are particularly attractive sclerochronological archives and can provide important contributions to paleoclimatic research (Aharon 1991; Watanabe and Oba 1999; Elliot et al. 2009; Batenburg et al. 2011; Welsh et al. 2011). In contrast to corals, they precipitate their shells in, or close to, isotopic equilibrium (Romanek and Grossman 1989; Aharon 1991; Elliot et al. 2009). Carbonate accretion takes place on a daily basis, which is recorded as microscopically visible growth increments in the shell structure (Aharon and Chappell 1986; Watanabe and Oba 1999; Sano et al. 2012). In the case of giant clams, bands grown during warm periods can usually be distinguished from those secreted during cold months, due to subtle color/density differences (Aharon 1991; Elliot et al. 2009; Welsh et al. 2011) and the resulting banding pattern thus provides a good lifespan control. Furthermore, *Tridacna* shell growth is fast, with growth rates from several mm/yr up to several cm/yr (Beckvar 1981; Aharon 1991; Elliot et al. 2009), which enables sampling and analysis at sub-seasonal time resolution. Moreover, *Tridacna* have a broad geographic distribution throughout the tropical and subtropical regions of the Indo-Pacific Ocean (Harzhauser et al. 2008; Hernavan 2012), and hence, are ideal low-latitude paleoclimate archives. However, well-preserved giant clams from Miocene strata are rare and so are corresponding studies (Batenburg et al. 2011). Despite their dense structure, diagenetic processes like neomorphism and cementation (enhanced by bioerosion) can affect the aragonitic shell structure. Very little work has been done on *Tridacna* shell diagenesis (Moir 1990; Faylona et al. 2011) and its impact on the original shell geochemistry.

Here, we present results from *Tridacna* shells of late Miocene (Tortonian) age from East Kalimantan, Indonesia. Our multi-proxy approach utilizes spatially resolved laser ablation–inductively coupled plasma-mass spectrometry (LA-ICPMS) element/Ca ratios (Mg/Ca, Sr/Ca, Ba/Ca) and microsampled $\delta^{18}O/\delta^{13}C$ records, which are aligned with the shell-banding pattern. Our primary aims are (1) to evaluate the fidelity of Miocene shells as paleoclimate archives by assessing their preservation, (2) to investigate how climate and paleoenvironmental proxy data contained within the shells can be extracted (3) to assess what information they contain about Miocene seasonality.

MATERIAL AND METHODS

The samples were obtained from the eastern coast of Borneo in the Indonesian province of East Kalimantan, close to the city of Bontang (Fig. 1). The two *Tridacna* shells studied herein were collected in December 2010 from outcrops TF108 (0° 11′ 7.08″ N, 117° 26′ 47.04″ E) and TF109 (0° 11′ 11.40″ N, 117° 26′ 40.92″ E). The outcrops are situated in close proximity to each other (~250 m distance) and at equal elevation (within GPS accuracy). A detailed overview of the Bontang area including TF localities 108 and 109 is provided in Renema et al. (2015). Both outcrops (Fig. 1) contain a rich, reef-associated fossil fauna embedded in light-brown, clay-rich Miocene carbonate sediments. Owing to their low permeability, clay-rich sediments provide a natural sealing for carbonate fossils (Pearson et al. 2001) and thus help facilitate excellent fossil preservation.

Biostratigraphic data, based on large benthic foraminifera and calcareous nannoplankton, indicate an early Tortonian (late Miocene) age for the studied strata in the Bontang area (Renema et al. 2015). Stratigraphically, the fossiliferous sediments of TF108 overlie those of TF109, with ~25 m of sediment in between.

The exteriors of both *Tridacna* shells are morphologically and mineralogically altered, resulting in the loss of important morphological features, such as fine details of the ribbing pattern and the hinge area (Fig. 2A, B). Thus, TF109LGS1 (further referred to as LGS1) was not identifiable to the species level. Shell TF108BW4B (further referred to as BW4B) is characterized by general elongate, low egg-shape, subtrigonal outline with widely spaced, low-wavy ribs, resembling those of *Tridacna derasa* (Röding 1798). However, the altered shell exterior prevents confident species identification. Both specimens are reposited in the collections of the Department of Earth Sciences, Natural History Museum, London (NHMUK), with the following registration numbers; PI TB 14531 (BW4B) and PI TB 14532 (LGS1).

To remove organic matter and sediment particles from external shell parts, the *Tridacna* shells were thoroughly cleaned using deionized water and a toothbrush. The valves were then cut along their maximum growth axis, from the umbo to the ventral margin (Fig. 2C, D).

Strontium Isotope Stratigraphy (SIS)

SIS was performed on seven *Tridacna* shells and four associated scleractinian corals (family Faviidae) in order to confirm the biostrati-

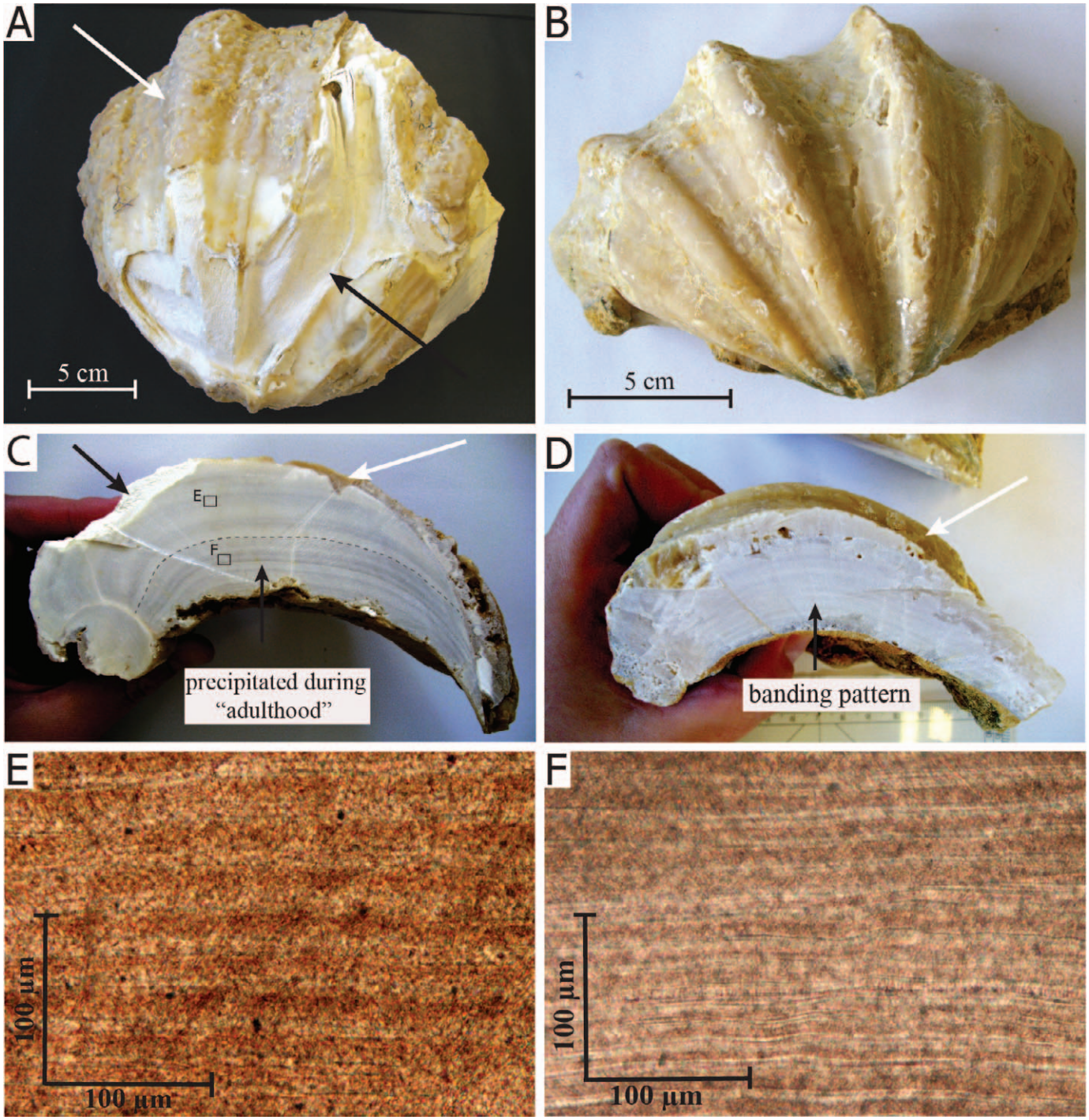

FIG. 2.—Photographs of whole and sectioned valves of BW4B and LGS1 and micrographs of daily growth increments of LGS1. **A)** Valve of LGS1; white arrow indicates presence of calcite, black arrow indicates altered aragonite. **B)** Valve of BW4B with completely recrystallized outer shell layer. **C)** Cross section of LGS1; white arrow indicates calcite, black arrow indicates altered aragonite. Gray dashed line marks the assumed transition between shell bands formed during juvenile phase and those secreted during the adulthood. **D)** Cross section of BW4B; white arrow indicates calcite; internal shell parts reveal a banding pattern. **E)** Daily growth increments of LGS1 secreted during juvenile phase, approximate position indicated in Part C. **F)** Daily growth increments of LGS1 secreted during adulthood, approximate position indicated in Part C.

graphically determined age estimates for the sampled fossil horizons from the Bontang area (Renema et al. 2015). The samples are derived from six different localities (TF 102, 108, 109, 110, 154, and 502), all situated west of the city of Bontang (Fig. 1B) and within a maximum distance of six km to each other.

Carbonate powders weighing between 5–100 mg were produced using a hand drill fitted with a 1 mm drill bit. Wet geochemistry procedures for Sr purification included dissolution in concentrated HNO_3, acidic rediges-tion in 4 M HNO_3 and extraction chromatography using Eichrom® Sr-spec resin (30 mg). Sr was loaded onto degassed single rhenium filaments,

TABLE 1.—*LA-ICPMS operating conditions.*

ICPMS parameters	Agilent 7500ce
RF power	1140–1320 W
Carrier gas flow (Ar)	0.53–0.67 l/min
Sampler, skimmer cones	Ni
Extraction lenses	ce
Monitored masses (m/z)	11, 23, 24, 25, 27, 31, 43, 55, 65, 66, 85, 89, 111, 138, 139, 140, 208, 238
Tuning parameters	$^{232}Th/^{238}U > 95\%$; $^{248}ThO/^{232}Th < 0.5\%$
Laser ablation system	Resolution M-50 (prototype)
He gas flow	850 ml/min
H_2 gas flow	8.5 ml/min
Laser repetition rate	15 Hz
Laser spot size	57 μm

preconditioned with H_3PO_4 and tantalum emitter after Birck (1986). $^{87}Sr/^{86}Sr$ ratios were measured on a VG354 multicollector thermal ion mass spectrometer (TIMS) in multidynamic mode (Thirlwall 1991) at RHUL. Control over mass fractionation for all measured ratios was guaranteed by normalization to the $^{86}Sr/^{88}Sr$ ratio of 0.1194. The long-term mean (2011–2012; n = 97) of measured $^{87}Sr/^{86}Sr$ of the international standard NIST SRM 987 is 0.710256 ± 0.000020 (2 SD). All data were corrected relative to the adopted NIST SRM 987 $^{87}Sr/^{86}Sr$ ratio of 0.710248. Resultant $^{87}Sr/^{86}Sr$ ratios were converted into their respective numerical ages by cross-correlation with the strontium isotope data set of the SIS Look-Up Table Version 4: 08/04 (McArthur et al. 2001; McArthur and Howarth 2004). Age minima and maxima were calculated by combining the statistical uncertainty of the SRM 987 long-term reproducibility (2 SD) with the upper and lower confidence limit reported with each Sr isotope ratio in the SIS Look-Up Table.

Scanning Electron Microscopy (SEM) and Cathodoluninescence (CL) Imaging

SEM was applied to investigate the morphology and crystalline structure of well-preserved and diagenetically altered shell domains. Uncoated samples were investigated using a LEO 1455 variable pressure (VP) SEM (operated at 15 kV) utilizing a solid-state 4 quadrant backscattered electron (BSE) detector and a Quanta 650 ESEM FEG used in VP mode with air as the imaging gas (operated at 7 kV) at the Natural History Museum, London. To enhance visibility of structural morphology, some samples were etched using acetic acid (different concentrations up to 5%, and different reaction times up to 30 min). High-quality digital imaging was performed using the LEO 1455 up to a magnification of 1200× and using the Quanta 650 up to a magnification of 4000×. Polished thin sections of shell cross sections were examined by cold CL microscopy using a Technosyn 8200 MkII luminoscope connected to a Nikon Optiphot petrological microscope at Royal Holloway University of London (RHUL).

X-Ray Diffraction (XRD)

XRD was conducted to determine the mineralogical structure of targeted shell domains. Powdered samples were produced by hand drilling and grinding (using mortar and pestle). Analyses were conducted on a few mg of shell carbonate using a Philips PW1830/3020 spectrometer with Cu Kα radiation, operated at 40 kV. Diffraction angles (2θ) between 25° and 37° were scanned, which include the main peaks of the $CaCO_3$ polymorphs calcite and aragonite. The limit of detection is typically better than 3%.

Laser Ablation–Inductively Coupled Plasma–Mass Spectrometry (LA-ICPMS)

Trace element variability was investigated using LA-ICPMS. Shell cross sections were cut to fit into the LA-ICPMS sample holder (49.5 mm × 27.5 mm × 7 mm) using a water-cooled Jencons Tyslide diamond saw. In order to produce a smooth sample surface and to enhance the visibility of growth increments, sample slabs were polished using silicon carbide paper (Buehler) on a rotating disk. Continuous trace element/Ca ratio profiles were obtained at RHUL using a 193 nm ArF excimer laser ablation system (Resolution M-50 prototype, Resonetics LLC, U.S.A.) featuring a Laurin two-volume laser ablation cell connected to an Agilent 7500ce quadrupole ICPMS (Müller et al. 2009). The LA-ICPMS operating conditions and monitored isotopes are given in Table 1. Shell material was ablated (following the preablated path) using a spot size of 57 μm, ablation speed of 1.8 mm/min and repetition rate of 15 Hz. To ensure a clean sample surface, preablation in two passes was performed (spot diameter of 74 μm, ablation speed of 6 mm/min, repetition rate 25 Hz). ^{43}Ca was used for internal standardization. Data reduction broadly followed Longerich et al. (1996) and was performed using Iolite run under Igor Pro (WaveMetrics, Inc., version 6.22A). NIST SRM 612 (Jochum et al. 2011a) was used as external standard and analyzed before and after each sample. The MPI-DING glasses GOR132-G, GOR128-G, and KL2-G were treated as unknowns and analyzed with each sample. Analytic accuracy was assessed by comparing the measured elemental abundances with the known and certified values of these standards (Jochum et al. 2011b). The samples were analyzed over a period of 6 months. Mean analytical accuracy (%) was 7.0, 4.0, 1.0, 10.5, 2.2, and 7.6 for B, Mg, Sr, Ba, La, and Ce, respectively.

Continuous traverses were analyzed perpendicular to visible growth bands to monitor the variability of trace elemental composition through time (time-series analysis). Ablation was performed from the inner shell edge (formed later in the life of the bivalve/ontogenetically older shell part) to the external rim of the shell (formed earlier in the life of the bivalve/ ontogenetically younger shell part).

Stable Isotope Analysis

Powdered aragonite samples were recovered from polished shell slabs using a semiautomated New Wave micromill fitted with a 300 μm drill bit. Single grooves with a length of 2 mm, depth of 360 μm, and width of 200 μm were milled parallel to existing growth bands in continuous mode. The powdered samples (300–400 μg) were analyzed for carbon and oxygen isotope ratios using a Micromass Multiflow head space system connected to a GV Instruments Isoprime IRMS at RHUL. After digestion in 103% orthophosphoric acid at 90 °C and a minimum of four hours reaction time, the evolved CO_2 was expanded into the sample loop and then delivered to the Isoprime mass spectrometer within continuous He-carrier gas flow. Each sample and standard was analyzed twice. Averaged precision (1 SD) of duplicates was 0.04‰ for $\delta^{18}O$ and 0.03‰ for $\delta^{13}C$. Standards used are NBS-19 and LSVEC international standards and an in-house standard (RHBNC calcite). Isotopic ratios are calibrated against these standards and expressed in conventional delta notation per mil values.

RESULTS

The results of sample imaging, XRD, and (isotope) geochemical analysis are displayed in Figures 2 to 10 and summarized in Tables 2 and 3.

Macroscopic and Microscopic Observations

The two shells studied, BW4B and LGS1, are visually affected by diagenetic alteration in their external shell parts (Fig. 2A, B). LGS1

TABLE 2.—*$^{87}Sr/^{86}Sr$ isotope ratios from 7* Tridacna *shells and 4 coral skeletons and data obtained from altered shell parts of BW4B and LGS1. Reported age estimations are derived from correlation with best fit data from SIS Look-Up Table V4: 08/04 (McArthur et al. 2001; McArthur and Howarth 2004). Errors result from the statistical uncertainty of the SRM 987 external reproducibility (±0.000020) combined with the upper and lower confidence limit of the respective "best fit" data.*

Tridacna/Coral sample	Measured $^{87}Sr/^{86}Sr$ ± 2SD	Resultant age (Ma)	+ error (Ma)	- error (Ma)
TF108BW4B (*Tridacna*)	0.708903 ± 11	9.75	0.39	0.37
TF109LGS1 (*Tridacna*)	0.708921 ± 11	9.16	0.65	0.46
TF08BW6 (*Tridacna*)	0.708921 ± 11	9.16	0.65	0.47
TF109WM (*Tridacna*)	0.708910 ± 09	9.55	0.48	0.38
TF110BW3 (*Tridacna*)	0.708930 ± 10	8.75	1.00	0.57
TF108BW10 (*Tridacna*)	0.708910 ± 12	9.55	0.48	0.38
TF108BW (*Tridacna*)	0.708897 ± 10	9.92	0.38	0.38
TF102BW1 (Coral)	0.708939 ± 11	8.24	0.92	0.71
TF154BW7 (Coral)	0.708903 ± 11	9.75	0.39	0.37
TF102BW2 (Coral)	0.708911 ± 09	9.52	0.50	0.38
TF502NS7 (Coral)	0.708905 ± 10	9.70	0.41	0.37
TF108BW4B calcite	0.708919 ± 11	9.25	0.64	0.43
TF109LGS1 calcite	0.708930 ± 11	8.75	1.00	0.57
TF109LGS1 sec. aragonite	0.708909 ± 11	9.58	0.46	0.38

contains calcified domains and also zones of a relatively porous, friable aragonite microstructure, which is henceforth referred to as altered aragonite (Fig. 2A, C). The outermost shell rim (~5–10 mm) of BW4B is completely recrystallized (Fig. 2B, D). However, both shell cross sections reveal an internal shell structure that to a large extent seems excellently preserved, and which is characterized by a distinct banding pattern, formed by alternating dark-light bands (Fig. 2C, D).

Light observations reveal that bands which appear relatively dark using reflected light illumination are most translucent/least dense, and therefore, appear bright under transmitted light, whereas bands which appear light using a reflected light source are least translucent/most dense, and therefore, appear dark under transmitted light. The literature shows inconsistencies concerning the use of terms such as "dark bands" resulting from observation using either transmitted (e.g., Aharon 1991; Watanabe et al 2004; Welsh et al. 2011) or reflected light illumination (e.g., Aubert et al. 2009; Batenburg et al. 2011). Optical descriptions of the presented shells herein refer to reflected light illumination.

Each dark-light couple likely represents a single year, which has been demonstrated for other *Tridacna* specimens (Aharon 1991; Elliot et al. 2009; Batenburg et al. 2011). Daily growth increments within the annual growth bands have been reported before (Watanabe and Oba 1999; Watanabe et al. 2004; Sano et al. 2012) and similarily can be identified in these late Miocene *Tridacna* shells using petrographic microscopy (Fig. 2E, F).

Both annual and daily growth bands indicate nonlinear growth through the lifetime of the *Tridacna* individual LGS1 (Fig. 2C, E, F), resulting in unevenly spaced time series. This Miocene clam is characterized by a rapid rate of growth and increase in shell thickness when younger (and presumably juvenile or subadult) which abruptly transitions into a phase characterized by much lower rates of shell secretion, that can be inferred to have been secreted during adulthood (Aharon 1991; Jones et al. 1986; Elliot et al. 2009). This is especially obvious when comparing the thickness of daily growth increments obtained from what we have labelled as juvenile and adult shell parts

TABLE 3.—*$\delta^{18}O_{shell}$ maxima, minima, and averaged values and respective calculated paleotemperature data of LGSI and BW4B. For comparison, published data of a Miocene* Tridacna gigas *(Batenburg et al. 2011) and corresponding paleotemperature and paleoseasonality estimates are presented. Paleotemperature/paleoseasonality was assessed using the aragonitic oxygen isotope temperature equation by Grossman and Ku (1986) and assuming $\delta^{18}O_{sw} = -0.88‰$.*

	$\delta^{18}O_{shell}$ min (‰)	$\delta^{18}O_{shell}$ max (‰)	average $\delta^{18}O_{shell}$ (‰)
LGS1	−2.90	−1.46	−2.15
BW4B	−3.00	−1.59	−2.31
Batenburg data	−2.97	−1.72	−2.30
	T (°C) max	T (°C) min	average T (°C)
LGS1	31.28	24.54	27.78
BW4B	31.75	25.13	28.52
Batenburg data	31.60	25.74	28.50
	average $\delta^{18}O_{shell}$ min (‰)	average $\delta^{18}O_{shell}$ max (‰)	
LGS1	−2.66	−1.69	
BW4B	−2.62	−2.05	
Batenburg data	−2.53	−2.09	
	average T (°C) max	average T (°C) min	**average seasonality** T (°C)
LGS1	30.17	25.60	**4.57**
BW4B	29.96	27.27	**2.69**
Batenburg data	29.54	27.47	**2.07**

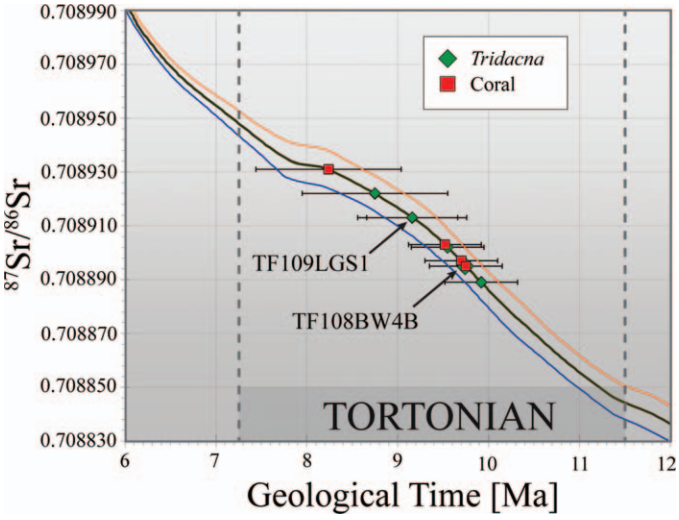

FIG. 3.—$^{87}Sr/^{86}Sr$ data of 7 *Tridacna* shells and 4 coral skeletons from the Bontang area (including results for LGS1 and BW4B) plotted versus the Sr isotope seawater curve based on the best fit data (black curve) from SIS Look-Up Table V4: 08/04 (McArthur et al. 2001; McArthur and Howarth 2004). Note that due to overlapping ratios (see Table 2) not all results can be displayed. Error bars indicate age minima and maxima, which were calculated by combining the statistical uncertainty of the SRM 987 long-term reproducibility (2 SD) with the upper (orange curve) and lower confidence limit (blue curve) reported with each Sr isotope ratio in the SIS Look-Up Table.

(Fig. 2E, F). While a distance of 100 µm corresponds to ~5 dark-light daily couplets in the juvenile shell parts (Fig. 2E), the same distance covers at least 8 dark-light daily couplets in shell parts secreted during the adult stage (Fig. 2F), representing a thickness of presumed individual daily growth increments of ~20 µm during the juvenile phase and ~12 µm during adulthood. A similar ontogenetic trend has been described in other giant clam shells (Aharon 1991; Watanabe et al. 2004; Elliot et al. 2009).

Strontium Isotope Stratigraphy

Seven *Tridacna* shells and four accompanying fossil corals from various localities with slightly different stratigraphic positions within the Bontang area (Renema et al. 2015) were selected for Sr isotope analysis. Resultant $^{87}Sr/^{86}Sr$ ratios with corresponding ages and errors are reported in Table 2 and Figure 3. The $^{87}Sr/^{86}Sr$ ratios of these individuals range between 0.708939 to 0.708897, representing ages of 8.24 to 9.92 Ma. These results clearly place the fossil assemblage into the Tortonian stage (7.25–11.61 Ma) and support biostratigraphically determined ages reported in Renema et al. (2015). The $^{87}Sr/^{86}Sr$ ratios of shells BW4B (0.708903) and LGS1 (0.708921) are identical within standard reproducibility.

To investigate the influence of diagenetic alteration on the Sr isotope ratio, clearly altered shell parts of BW4B (calcite) and LGS1 (calcite and secondary aragonite) were targeted (Table 2). Resultant $^{87}Sr/^{86}Sr$ ratios obtained from pristine aragonite and respective Sr isotope ratios from calcite and secondary aragonite respectively are identical within limits of analytical uncertainty (Table 2).

SEM and CL Imaging

Pristine aragonite consists of a crossed-lamellar, highly ordered structure (Fig. 4A, C, E, H). Single lamellae are relatively short (<10 µm) but elongate, lathlike crystals, that are inclined at nearly right angles (Fig. 4C). The tightly interlocked crystals build a very dense and solid microstructural framework. This kind of shell structure is common for aragonitic shells, including *Tridacna* specimens (Taylor et al. 1973; Moir 1990; Faylona et al. 2011). Pristine aragonite of BW4B shows patchy dissolution, "melted-like" structures (Fig. 4H), which have been reported as a sign of early recrystallization (Faylona et al. 2011).

The altered aragonite of LGS1 reveals a crossed-lamellar arrangement (Fig. 4D), similar to pristine aragonite. However, there are differences in crystal size and morphology and general shell fabric compared to pristine aragonite. The altered aragonite crystals are much larger, up to 20 µm in length (Fig. 4D, F). They are thinner and porous (Fig. 4F), which makes them friable. Furthermore, the crystals are bent, resulting in a disordered, wavelike shell structure containing cavities (Fig. 4D). Diagenetic calcite appears predominantly in the outermost rims of both shells (Fig. 4A) and is characterized by large blocky crystals, which are broken (in a stepwise manner) along their rhombohedral cleavage planes (Fig. 4B, G).

Both light and dark bands are characterized by the crossed-lamellar structure typical for pristine aragonite as described above. The formation of the banding pattern is therefore not due to structural differences. Welsh et al. (2011) suggest that dark (translucent, low-density) shell bands consist of larger crystals relative to bright bands (less translucent, high density), which seems plausible, assuming that tightly joined small crystallites will build a denser shell structure compared to fewer, larger crystallites. However, a significant difference in the size of the individual crystallites within dark and bright bands could not be resolved using SEM.

Cathodoluminescence images of pristine aragonite zones obtained from both shells reveal dark-blue luminescence (Fig. 5A, B). While LGS1 is characterized by a homogeneous blue color, bright patchy "stains" are more frequent in BW4B and additionally a single green luminescing (growth) band can be identified (Fig. 5B). Calcite at the rims of LGS1 and BW4B is characterized by blue to slightly purple luminescence (Fig. 5C, D). Specimen BW4B additionally reveals coexisting calcite zones characterized by distinct brighter, purple-pink luminescence (Fig. 5D). CL imaging did not result in better visibility of the dark-light banding pattern. Macroscopically visible dark and light bands appeared dark and light in CL mode, and no color change or distinct difference of luminescence intensity could be observed.

XRD Analyses

XRD analyses were performed on the Miocene shells, targeting well-preserved as well as altered shell domains. Hand-drilled sample powders obtained from internal shell parts (pristine aragonite) of LGS1 produced major peaks at diffraction angles (2θ) of 26.2° and 27.2°, and minor peaks at angles of 33.2° and 36.2°, all indicating aragonite (Fig. 6A). Altered aragonite from sample LGS1 produced a similar XRD spectrum to that obtained from unaltered crystals (Fig 6A).

Microscopically visible blocky calcite of both shells produced one major peak at 29.4°–29.5° 2θ typical for calcite (Fig. 6A, B). XRD analysis of ground powder recovered from the internal, visibly well preserved shell parts of BW4B revealed 100% aragonite composition (Fig. 6B). Hand-drilled shell powder of BW4B contained about 10% calcite (Fig. 6B), whose significance is discussed below.

LA-ICPMS Profiles

Chemical Signatures of Shell Mineralogical Domains.—LA-ICPMS analysis along a track covering both primary and altered aragonite of sample LGS1 revealed significant geochemical difference between these two domains (Fig. 7). The monitored element/Ca ratios (Mg/Ca, Sr/Ca, Ba/Ca, Mn/Ca, Al/Ca, La/Ca, and Ce/Ca) are either highly elevated or show a pronounced high-frequency variability in the area comprised of altered aragonite. At a distance of ~30 mm from the inner shell edge Mn/Ca, Al/Ca, La/Ca, and Ce/Ca increase up to two orders of

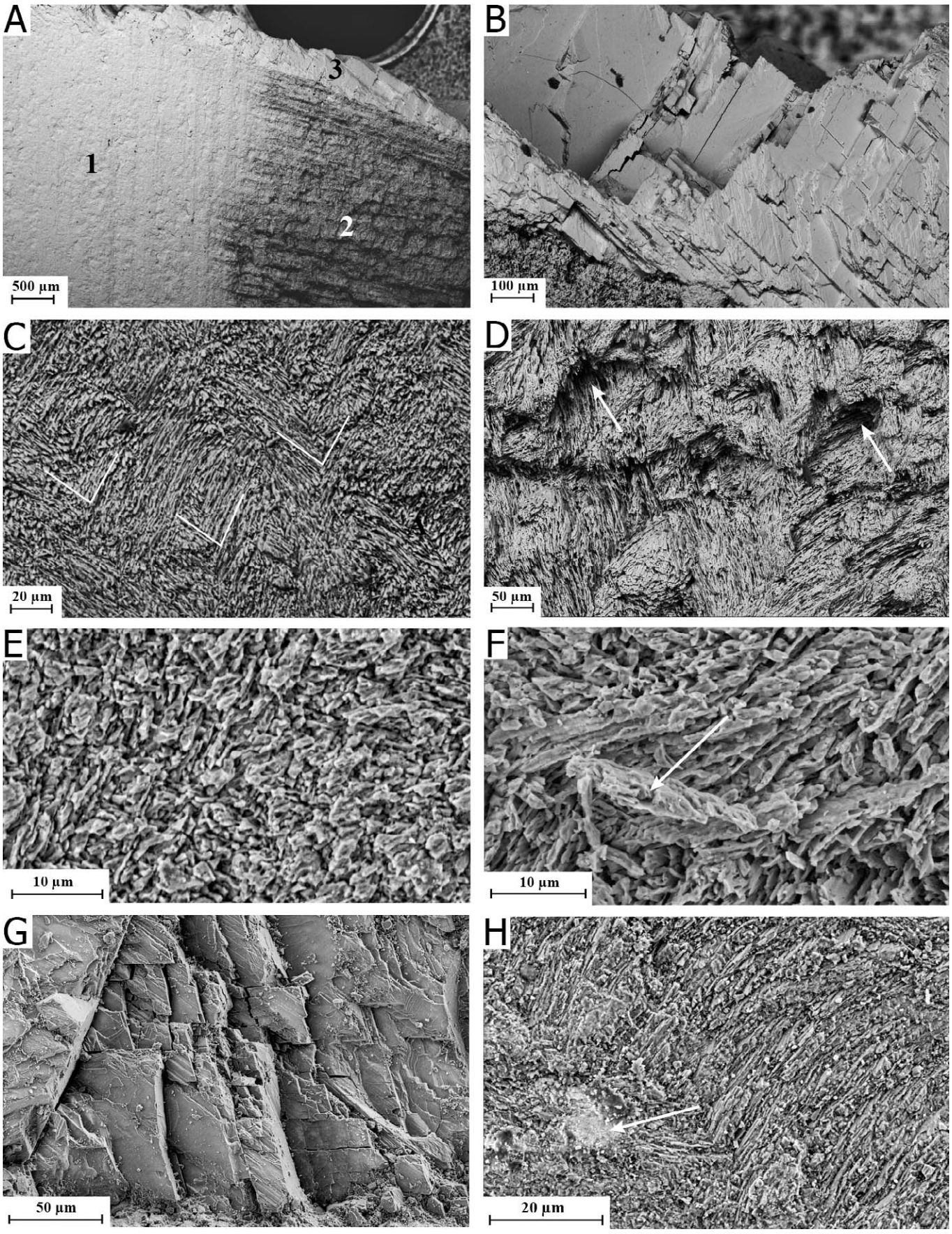
A
1
2
3
500 µm
B
100 µm
C
20 µm
D
50 µm
E
10 µm
F
10 µm
G
50 µm
H
20 µm

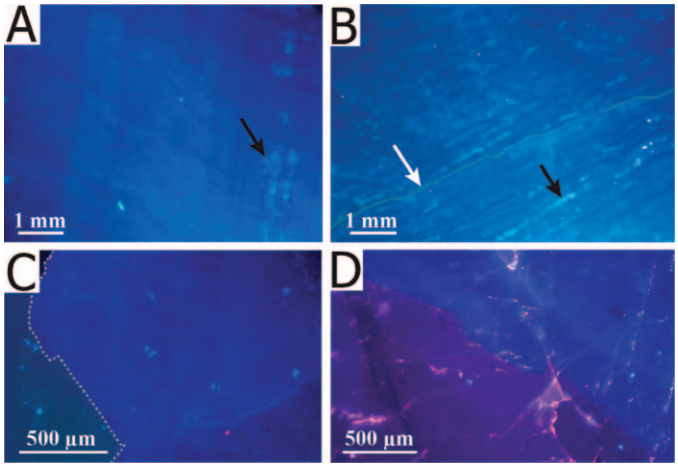

FIG. 5.—Cathodoluminescence images of aragonite and calcite of both shells. **A)** Dark-blue intrinsic luminescence of LGS1 indicates excellent preservation of aragonite. Occurrence of brighter patchy stains indicated by black arrow. **B)** Slightly higher luminescing aragonite of BW4B. Thin green growth band (marked with white arrow) indicates higher Mn^{2+} concentrations in this area. Bright patchy stains marked by black arrow. **C)** Intrinsic blue luminescence of calcite for LGS1, dashed line marks border between thin section and underlying glass slide. **D)** Calcite of BW4B characterized by two different luminescence colors. Blue indicates very low Mn^{2+} contents, whereas elevated Mn^{2+} concentrations activate the pink luminescence.

magnitude. This coincides with the macroscopically visible transition from pristine to altered aragonite (Fig. 7). It is therefore possible to align the trace elemental record with the macroscopic observations. The transition from "normal" aragonitic values to elevated ratios in the altered zone is sharp. From ~32 mm distance from inner shell edge onward Mg/Ca, Sr/Ca, and Ba/Ca ratios are characterized by a noisy high-frequency signal.

The LA-ICPMS profiles obtained from a track that covers pristine aragonite and the adjacent calcitic zone of shell BW4B reveal that aragonite is an order of magnitude enriched in B/Ca, Sr/Ca, and Ba/Ca and depleted in Mg/Ca, Mn/Ca, La/Ca, and Ce/Ca relative to calcite (Fig. 8).

At a distance of ~16 mm from inner shell edge, the laser ablation (LA) track intersects the macroscopically visible border between aragonite and calcite. Almost all monitored elemental ratios reveal a distinct and sharp compositional change at this distance. The two covarying rare earth elemental ratios (La/Ca and Ce/Ca), however, steadily increase from ~14 mm onward.

Mg/Ca.—The Mg/Ca ratio of LGS1 varies from about 0.4 to 1.4 mmol/mol (Fig. 9; see supplemental data). Even though the variation is not regular, an oscillatory pattern can be identified. Alignment of the Mg/Ca record with the shell-banding pattern reveals that high Mg/Ca ratios correspond to dark growth bands, while lower Mg/Ca ratios match with lighter growth bands (Figs. 7, 9). A gentle increase in the Mg/Ca ratio and in amplitude of the Mg/Ca record toward ontogenetically older shell parts (secreted during adulthood) produces oscillations characterized by overall higher Mg/Ca ratios with greater amplitude for the first ~16 mm of the profile.

The Mg/Ca ratio of BW4B ranges from about 0.4 to 1.0 mmol/mol (Fig. 10; see supplemental data). Alignment of the Mg/Ca profile and the banding pattern is possible for the last ~10 mm of the profile, with high Mg/Ca corresponding to dark growth layers (Fig. 10). However, compared to LGS1, the alignment is not as clear and is not constant throughout.

Sr/Ca.—The ratio of Sr/Ca of LGS1 varies from ~1.5 to 3.5 mmol/mol (Fig. 9). Overall, the profile reveals irregular variability. An oscillation pattern or ontogenetic trend as described for Mg/Ca of LGS1 cannot be seen. There is no covariation of ratios with the shell-banding pattern.

The Sr/Ca profile of BW4B ranges from about 1.7 to 2.9 mmol/mol and is characterized by high-amplitude/low-frequency variability (Fig. 10; see supplemental data). A reasonable fit exits between dark growth bands and elevated Sr/Ca ratios (Fig. 10). The Mg/Ca and Sr/Ca ratios covary slightly from ~7 mm distance from inner shell edge onward.

Ba/Ca.—The Ba/Ca values range between about 0.3 to 1.4 µmol/mol and 0.6 to 1.8 µmol/mol for LGS1 and BW4B, respectively (Figs. 9, 10). Corresponding profiles of both *Tridacna* shells are characterized by fine-scale, low-amplitude/high-frequency variability (Figs. 9, 10), that do not correspond with the shell-banding pattern.

Stable Isotope Profiles

$\delta^{18}O$.—The stable isotope profile of LGS1 (Fig. 9) is based on 188 analyses (resolution 200 µm) covering a distance of 37.6 mm. The $\delta^{18}O$ values range from −2.90‰ to −1.46‰ with an average value of −2.15‰ for LGS1 (Table 3). The $\delta^{18}O$ profile reveals pronounced variability and can be aligned with the shell-banding pattern. Dark bands correspond to low oxygen isotope ratios, whereas light bands match with high $\delta^{18}O$ values (Fig. 9).

The Mg/Ca and $\delta^{18}O$ profile of LGS1 are inversely correlated, with high Mg/Ca ratios corresponding to relatively light $\delta^{18}O$ values and low Mg/Ca ratios corresponding to heavy oxygen isotope ratios (Fig. 9). The two profiles correlate in great detail. As for Mg/Ca, a distinct change of amplitude and frequency occurs at ~16 mm distance from the inner shell edge. While the first 16 mm (shell parts secreted during adulthood) are characterized by high-amplitude/low-frequency variability, the final ~10 mm (shell parts secreted during juvenile stage) of the profile reveal low-amplitude/high-frequency variations.

The stable isotope profile of BW4B (Fig. 10) is based on 77 data points recovered from a shell length of 15.4 mm. The $\delta^{18}O$ values oscillate from −3.00‰ to −1.59‰ with an average value of −2.31‰. Alignment with the shell-banding pattern is possible. Light $\delta^{18}O$ values correspond to dark growth bands, while heavy $\delta^{18}O$ values match with light growth bands. Inverse correlation between the Sr/Ca profile and the $\delta^{18}O$ record

←

FIG. 4.—Scanning electron microscope images on the microstructures and diagenetic textures of LGS1 (A–F) and BW4B (G–H). **A)** Overview image of pristine aragonite (=1), altered aragonite (=2), and calcite (=3). **B)** Calcite at the shell rim characterized by typical rhombohedral cleavage planes. **C)** Pristine aragonite after etching in 5% acetic acid for 30 min. Dense, crossed-lamellar structure consisting of short lathlike crystals inclined at an angle of ~90° to each other (indicated with white strokes). **D)** Loosely packed, large and curved altered aragonite crystals which build a very coarse, wavelike structure resulting in cavities (marked by arrows). **E)** High-magnification micrograph of pristine aragonite. **F)** High-magnification micrograph of altered aragonite. Crystals range from 10 to 20 µm, are thin, and porosity (marked by arrow) is present. **G)** Diagenetic calcite at shell rim, which resembles the calcitic structure as described for LGS1 (see Part B). **H)** Pristine aragonite with similar structural characteristics as described for LGS1 (see Part E). Patch of dissolution, which is about 10 µm in diameter and might indicate incipient recrystallization (marked by arrow).

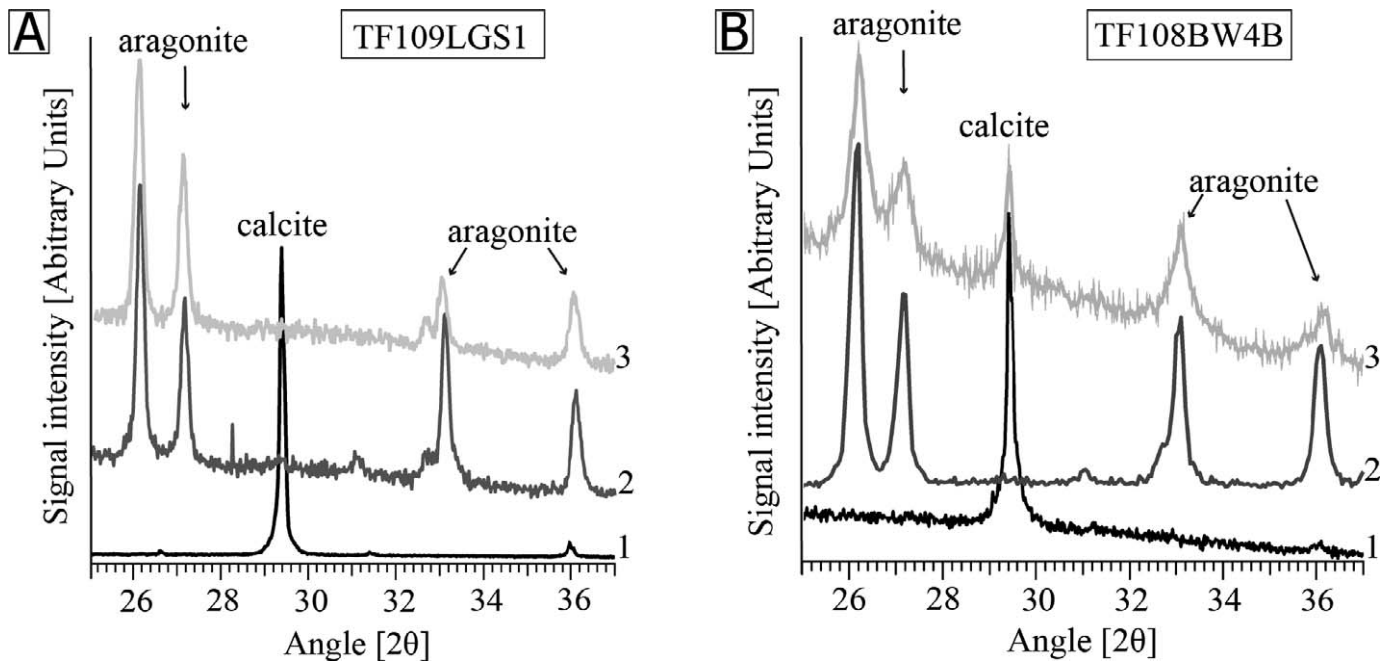

FIG. 6.—XRD spectra obtained from both *Tridacna* shells. **A)** LGS1: 1 = diagenetic calcite with one major peak at a diffraction angle of 29.4°, representing calcite. 2 = pristine aragonite and 3 = altered aragonite, both showing 4 major peaks at 26.2°, 27.2°, 33.2°, and 36.2°, representing aragonite. **B)** BW4B: 1 = diagenetic calcite with one major peak at a diffraction angle of 29.4°. 2 = ground sample from the internal parts of the shell, revealing pure aragonitic composition. 3 = drilled sample from the internal parts of the shell, characterized by peaks indicating the presence of both aragonite and calcite.

exists, however the agreement is not as good as for Mg/Ca and $\delta^{18}O$ in the case of LGS1.

Both shells reveal eight (best visible) dark-light couples that correspond to eight major $\delta^{18}O$ oscillations ($\delta^{18}O$ maxima and minima). These findings imply that both *Tridacna* specimens had lifespans of at least eight years.

$\delta^{13}C$.—The $\delta^{13}C$ values of LGS1 range between 0.32‰ and 2.45‰ with an average of 1.89‰ (Fig. 9). Overall, the profile is characterized by irregular variability, which does not align with the shell-banding pattern. Consequently, $\delta^{13}C$ and $\delta^{18}O$ do not correlate. Just as for the $\delta^{18}O$ signal, the frequency of peaks is higher for shell parts grown during the juvenile phase (from ~16 mm onward).

The $\delta^{13}C$ profile of BW4B shows pronounced oscillations varying from 1.68‰ to 3.2‰ with an average of 2.39‰ (Fig. 10). Eight major $\delta^{13}C$ oscillations (eight major $\delta^{13}C$ maxima and minima) are visible. An apparent negative correlation between $\delta^{13}C$ and $\delta^{18}O$ exists, especially from 4 mm distance from inner shell edge onward. However, a phase lag of a few weeks appears to exist between the two profiles.

DISCUSSION

Evaluation of Preservation and Implications For Retrieving Paleoenvironmental Information

Our multimethod approach combining macroscopic and microscopic observations, SEM/CL imaging, XRD analysis, and LA-ICPMS screening reveals that both shells contain altered zones (calcite and/or altered aragonite) as well as nonaltered parts (pristine aragonite). We exclude the possibility that such mineralogically manifested alteration is the result of changes during shell growth, because these features are not consistently present throughout the shells, but patchy in distribution. Following isochronous growth bands reveals that while at one position of the shell the given growth band is not modified, at another position the same growth band has been diagenetically transformed (Fig. 2C, D). We thus suggest that both calcite and altered aragonite are products of abiotic postmortem recrystallization. As such, alteration or diagenesis is used to refer to any modification of the mineralogy and composition of the original aragonitic biominerals.

SEM studies imply that the original aragonitic microstructure of LGS1 and BW4B is largely excellently preserved. Patchy dissolution features (Fig. 4H) were identified in BW4B, which might indicate incipient recrystallization (Faylona et al. 2011).

Both shells are characterized by dark-blue, dim cathodoluminescence (Fig. 5). Nonluminescent to blue luminescent colors in biogenic carbonates have been interpreted as an indicator for excellent preservation (Barbin et al. 1995; Gotte and Richter 2009; Brand et al. 2012; Wendler et al. 2012). The intrinsic luminescence is due to the absence of Mn^{2+}, which is a major luminescence activator in carbonates (Langlet et al. 2006). Elevated Mn^{2+} concentrations in aragonite result in yellow-green luminescing aragonite (Barbin et al. 1995; Gotte and Richter 2009). The single green band observed in BW4B (Fig. 5B) is therefore interpreted as composed of aragonite with an elevated Mn^{2+} content relative to the surrounding aragonite.

Mn^{2+} activates luminescence in calcite at longer wavelengths (Barbin et al. 1995) and depending on its concentration produces purple, red, or orange colors (Langlet et al. 2006). Blue to weak purple luminescing calcite obtained from the rims of LGS1 (Fig. 5C) indicates a pure $CaCO_3$ composition with only minor Mn^{2+} incorporation into the calcite lattice. Calcite of BW4B shows intrinsic blue luminescence and also areas with a distinct brighter, purple-pink luminescence (Fig. 5D), which indicates elevated Mn^{2+} concentrations in these calcite zones. CL imaging confirms the findings of SEM analysis, showing an excellently preserved original aragonite structure of LGS1 and an overall well preserved aragonitic microstructure of BW4B. The presence of similar XRD spectra for pristine and altered aragonite of LGS1 (Fig. 6A) demonstrates that XRD alone is not a sufficient tool for assessing the preservation state of

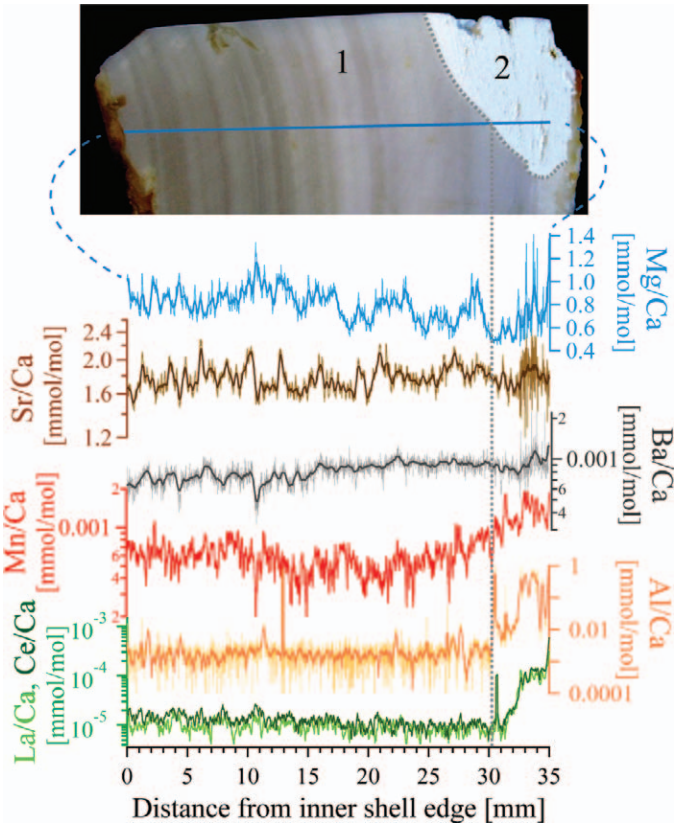

FIG. 7.—Polished thick section of LGS1, with position of laser transect and corresponding trace element profiles (presented on a logarithmic scale). Gray dotted line marks position where the laser-ablation track intersects the border between the well-preserved (=1) and altered aragonite (=2) structure at a distance of ~30 mm from inner shell edge. Smoothing was performed using moving average.

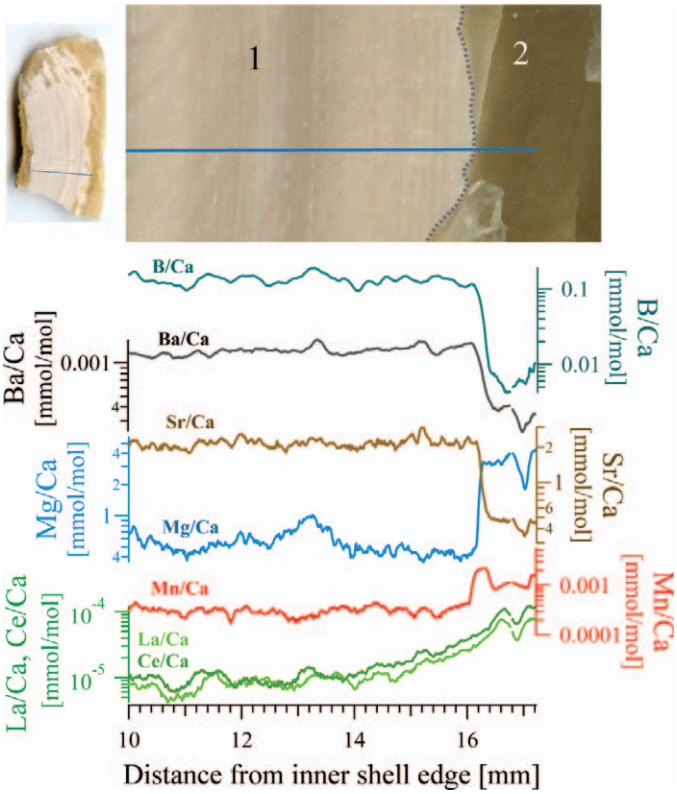

FIG. 8.—Polished thick section of BW4B, with position of laser transect and corresponding trace element profiles (presented on a logarithmic scale). Gray dotted line marks position were the laser-ablation track intersects the border between aragonite (=1) and calcite (=2) at a distance of ~16 mm from inner shell edge. Smoothing was performed using moving average.

aragonite. However, it is suitable to distinguish between the two carbonate polymorphs calcite and aragonite (Fig. 6A, B).

Ground samples obtained from the internal, well-preserved shell parts of BW4B revealed 100% aragonite composition, while hand-drilled samples obtained from the same shell parts contained ~10% of calcite (Fig. 6B). The latter contradicts the macroscopic observations and findings of SEM/CL imaging and LA-ICPMS analysis. None of these methods indicate the presence of calcite in the internal structure. Macroscopically, the banding pattern is preserved (Fig. 2D) and no large blocky crystals could be identified. SEM observations reveal a crossed lamellar structure (Fig. 4H), strikingly similar to that of LGS1 (Fig. 4C) and typical for bivalve aragonite. Cathodoluminescence images are characterized by blue luminescence (Fig. 5B), typical for pure biogenic aragonite. LA-ICPMS profiling does not imply significant compositional changes. Neither distinctively elevated Mg/Ca, La/Ca, Ce/Ca, Mn/Ca, nor significantly depleted Sr/Ca, B/Ca, Ba/Ca ratios, which characterize calcite recrystallization (Fig. 8), were detected. All these results support the interpretation of a well-preserved aragonitic structure in BW4B. Crucially, calcite was only detected in powdered samples produced via hand drilling, but not in those produced by grinding. Potential sample cross-contamination from adjacent calcite zones can be excluded, as repeated measurements were performed on previously cut, well-preserved, internal shell parts only. We conclude that conversion of aragonite to calcite occurred during the drilling process of XRD sampling. Calcite detected in hand-drilled samples from well-preserved internal shell parts can thus be interpreted as a sampling artifact and is not diagenetic in origin. Transformation of marine biogenic aragonite to calcite (up to 6%) due to heat and stress exposure during the drilling process has been reported before (Aharon 1991; Foster et al. 2008). Aharon (1991), who studied a *Tridacna gigas* specimen, additionally reported an offset in $\delta^{18}O$ values due to drilling. On the contrary, Foster et al. (2008) studied fish (cod) otoliths and concluded that micromilling did not affect $\delta^{18}O$ measurements in these specimens. The drilling-induced aragonite to calcite polymorph transition occurs in the case of BW4B, whereas no such sampling artifact is observed for LGS1, which might be related to minor microstructural differences. SEM analysis of BW4B revealed microdissolution features (Fig. 4H), possibly indicating incipient recrystallization. An overall weaker aragonite structure of BW4B might more readily convert during drilling than the more stable structure of LGS1. Even though microsamples for stable isotope analysis were obtained via micromilling (no hand drilling), a possible $CaCO_3$ polymorph transformation introduced by the milling process in case of BW4B cannot be excluded. But, since its $\delta^{18}O$ profile is characterized by a well-defined oscillatory pattern, which correlates with the banding pattern of the shell (Fig. 10), and furthermore, absolute $\delta^{18}O$ values are in good agreement with those of LGS1, we conclude that micromilling did not affect the stable oxygen isotope composition.

Several studies have applied trace elemental screening to coral skeletons in order to investigate the impact of diagenetic alteration on elemental composition and its resultant consequences for paleoenvironmental interpretations (Hendy et al. 2007; Hathorne et al. 2011; Sayani et al. 2011; Griffiths et al. 2013). Similar work focusing on the chemical composition of diagenetically altered shell areas of *Tridacna* are to our knowledge absent. The intrinsic multielemental capability of LA-ICPMS

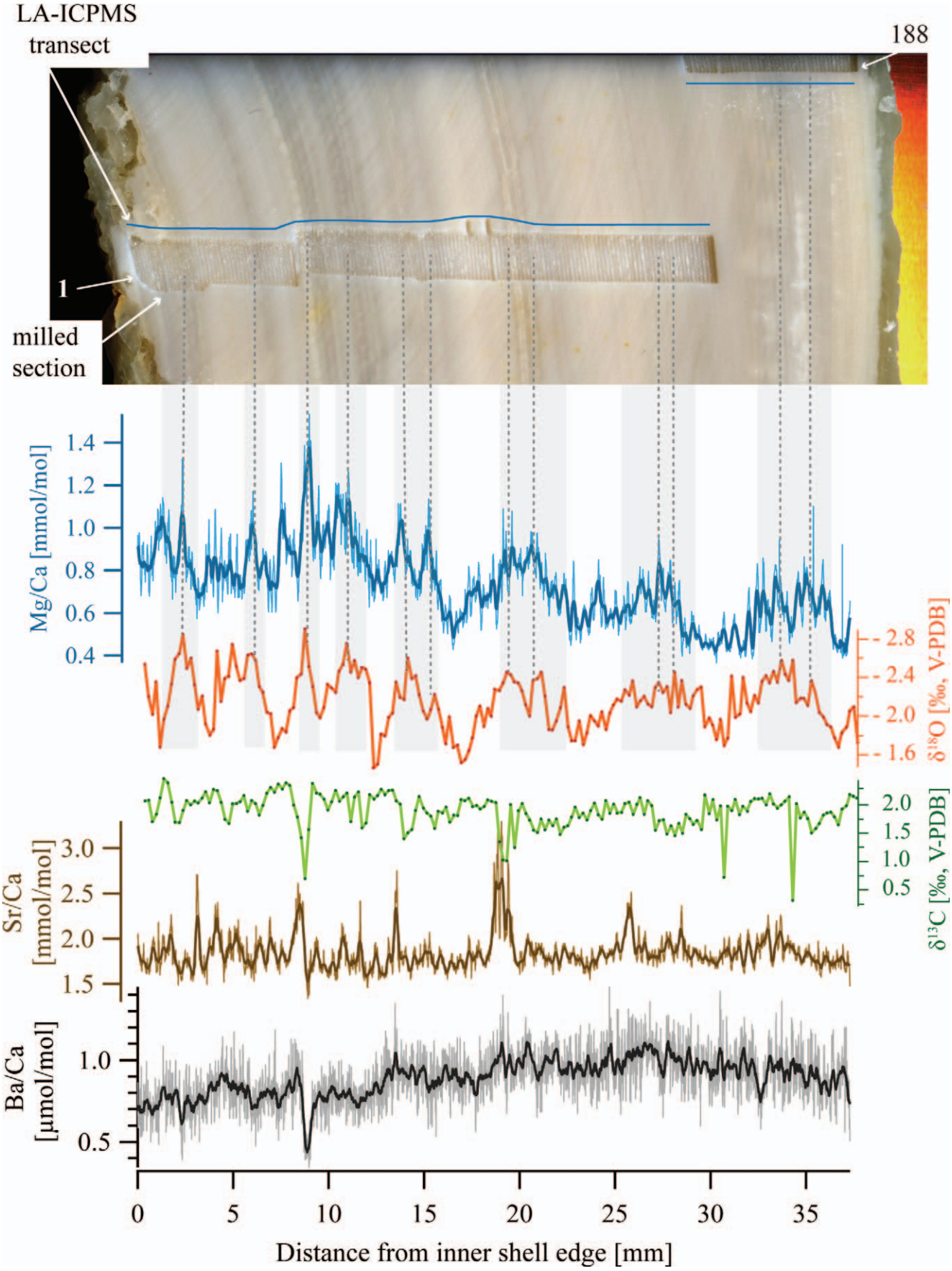
LA-ICPMS
transect
188
1
milled
section
Mg/Ca [mmol/mol]
1.4
1.2
1.0
0.8
0.6
0.4
δ18O [‰, V-PDB]
-2.8
-2.4
-2.0
-1.6
δ13C [‰, V-PDB]
2.0
1.5
1.0
0.5
Sr/Ca
[mmol/mol]
3.0
2.5
2.0
1.5
Ba/Ca
[µmol/mol]
1.0
0.5
0
5
10
15
20
25
30
35
Distance from inner shell edge [mm]

enables to monitor both "proxy" element/Ca ratios (e.g., Mg/Ca, Sr/Ca, Ba/Ca), as well as elements indicative of diagenesis (e.g., Mn, Al, REEs). Mn/Ca, Al/Ca, La/Ca, and Ce/Ca ratios change together with microstructures at about 30 mm distance from the inner shell edge (border between pristine aragonite to altered aragonite). The diagenetic monitor element/Ca ratios are distinctively enriched in altered aragonite relative to pristine aragonite. Elevated Mn concentrations in bivalve and brachiopod shells have been interpreted as an indication for diagenetic alteration (Grossman et al. 1996; Gomez-Alday and Elorza 2003). The elevated Al concentrations of the altered aragonite domain likely reflect the abundance of aluminum-bearing minerals in the cavities of this structure. Owing to the high porosity of the altered aragonite structure, the incorporation of interstitial minerals is facilitated. Indeed, XRD analysis of altered aragonite powder revealed the possible existence of diaspore (δ-AlO(OH)). This aluminum hydroxide is a typical weathering product of aluminosilicates in tropical regions and its occurrence is compatible with the clay-rich sediments in which the shells were found. Thus, the measured traces (<1%) of diaspore likely explain the enhanced Al concentrations detected via LA-ICPMS.

Significant compositional differences for the proxy element/Ca ratios Mg/Ca, B/Ca, Ba/Ca, and Sr/Ca were observed when comparing pristine aragonite versus diagenetic calcite (Fig. 8). While B/Ca, Sr/Ca, and Ba/Ca are strongly depleted, Mg/Ca is strongly enriched in diagenetic calcite compared to the pristine aragonite. Using proxy data obtained from those calcite zones for paleoenvironmental studies would result in unreliable inferences. All these ratios are prominent paleoenvironmental proxies (Mg/Ca, Sr/Ca: temperature; B/Ca: salinity/pH; Ba/Ca: runoff/upwelling, primary productivity). Calculating paleotemperature from those zones using, e.g., Mg/Ca and Sr/Ca would result in positive temperature anomalies.

Elemental incorporation into the carbonate structure is mainly controlled by the shell mineralogy. Relatively large cations like Sr^{2+} and Ba^{2+} substitute better for Ca^{2+} in the orthorhombic aragonite structure, while smaller ions such as Mg^{2+} show affinity to the rhombohedral calcite lattice (Gotte and Richter 2009). The behavior of Mg and Sr in the different carbonate polymorphs was documented by Harriss (1965), who compiled analyses of molluscan shell material of 95 different species. He reported overall lower Mg concentrations in aragonite (several hundred ppm) versus calcite (several thousand ppm), while Sr generally was found in higher concentrations in aragonite (frequency maximum at 2500 ppm) compared to calcite (frequency minimum at 1500 ppm). Diagenetic calcite cements in Miocene aragonitic coral skeletons have been found to be enriched in Mg/Ca and depleted in Sr/Ca relative to pristine aragonite by a factor of 15 to 20 (Griffiths et al. 2013).

To evaluate the impact of alteration on the Sr isotope ratio, diagenetic calcite from BW4B and calcite and secondary aragonite from LGS1 were compared with the respective ratios obtained from pristine zones. Due to the considerable Sr concentration changes documented by the LA-ICPMS, significant differences in the Sr isotope ratio between the different carbonate polymorphs were expected. However, considering the estimates of analytical uncertainty, pristine and altered zones show near identical $^{87}Sr/^{86}Sr$ ratios (Table 2). Two hypotheses are possible to explain this: (1) The effect of diagenetic alteration on the Sr isotope composition was small, hence the $^{87}Sr/^{86}Sr$ ratio has not resolvably been modified (considering the measuring inaccuracy and the error of the Sr isotope seawater curve). Simple loss of Sr without later admixture of isotopically different Sr also does not change the initially acquired $^{87}Sr/^{86}Sr$ isotope composition. (2) Diagenetic alteration either affected the living specimen (recrystallization from the same $^{87}Sr/^{86}Sr$ pool) or occurred relatively early postmortem, at a time interval that cannot be resolved in regard to the current measurement uncertainty for our geochronological dating (~ <1 Ma).

Ba/Ca Profiles: Lack of Phytoplankton Blooms?

Several recent studies treat environmental implications of barium shell geochemistry on modern marine bivalves (e.g., Gillikin et al. 2006, 2008; Elliot et al. 2009; Thébault et al. 2009). All report very similar high-resolution Ba/Ca profiles, which are characterized by large, sharp, periodically occurring Ba peaks of high intrashell and even interindividual reproducibility.

Ba/Ca signals in coral skeletons and planktic foraminifera are interpreted as proxies for riverine runoff (sediment flux) and upwelling of deep, nutrient-rich water (e.g., McCulloch et al. 2003; Chen et al. 2011; Hönisch et al. 2011; Grove et al. 2012). Studies on Ba/Ca variability in bivalve shells suggest a direct link between the presence of phytoplankton blooms/high phytoplankton activity and the Ba/Ca peaks (e.g., Lazareth et al. 2003; Gillikin et al. 2006, 2008; Elliot et al. 2009; Thébault et al. 2009); however, the mechanism of barium incorporation into the shell carbonate remains ambiguous (Elliot et al. 2009). Species-specific effects, which might influence barium uptake and incorporation into the shell structure, might also be relevant (Gillikin et al. 2008).

The Ba/Ca records preserved in the presented Miocene *Tridacna* shells discussed herein are different from modern profiles as described above. No pronounced Ba/Ca peaks can be identified, and overall these records are characterized by irregular variability (Figs. 9, 10). The low Ba/Ca variability in our specimens may indicate a lack of plankton blooms and/or stable euhaline conditions at the time of shell formation; however, the length of the *Tridacna* records is too short to exclude the presence of interseasonal variations in local primary productivity.

Seasonality Derived from LA-ICPMS and Stable Isotope Time-Series Profiles

Tridacna secrete their aragonitic structure in or close to isotopic equilibrium (Romanek and Grossman 1989; Aharon 1991; Elliot et al. 2009). The measured shell $\delta^{18}O$ is comprised primarily of two components: (1) $\delta^{18}O$ seawater ($\delta^{18}O_{sw}$), which is closely related to salinity/ice volume and (2) fractionation as a function of SST ($\delta^{18}O_{temp}$) (e.g., Aharon 1991). In regions with constant salinity, shell $\delta^{18}O$ can be interpreted as being temperature controlled.

Much of the coastline of East Kalimantan is subjected to riverine influence from the Mahakam delta, a fluvio-deltaic system that already existed during the Miocene. Salinity variation (e.g., reduced salinity due to fluvial runoff) negatively impacts on the relationship between corals and their symbionts (e.g., Moberg et al. 1997; Mayfield and Gates 2007), for which the occurrence of coral reefs is usually taken to indicate stable euhaline conditions. Since our studied shells were collected within a rich and diverse fossil coral community, we assume that shell formation took place under relatively constant sea-surface salinity (SSS) conditions.

←

FIG. 9.—Polished thick section of LGS1 used for stable isotope analysis, with positions of micromilled section and laser transect, and respective stable isotope and LA-ICPMS profiles. Micromilled section as indicated by arrows ranges from sample 1 (innermost shell edge) and sample 188 (outermost shell edge). Blue line represents laser-ablation track. Gray bars and dotted lines indicate good agreement between $\delta^{18}O$ and Mg/Ca and alignment with the shell-banding pattern. Smoothing of LA-ICPMS data was performed using the moving average.

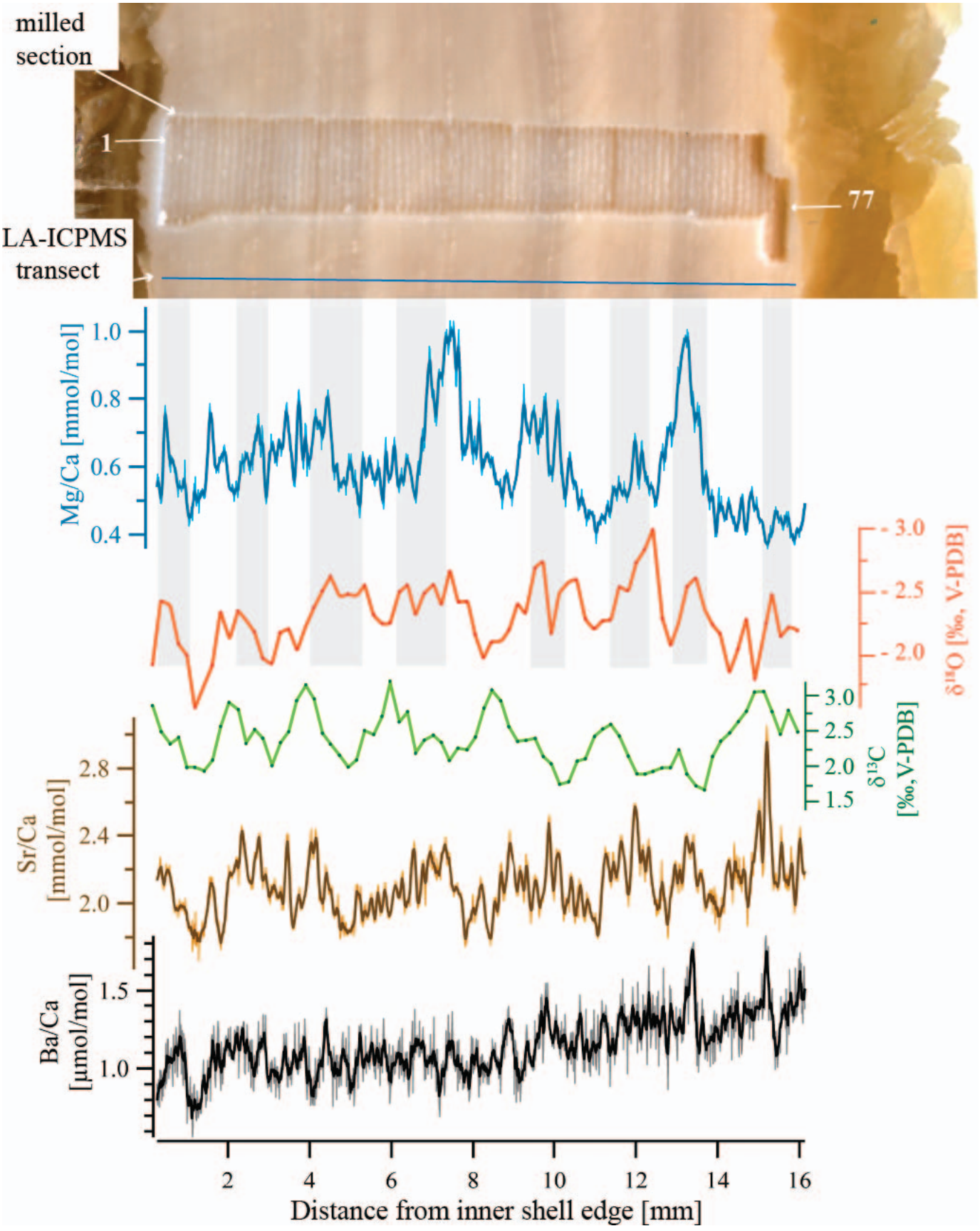
milled section
1
77
LA-ICPMS transect
Mg/Ca [mmol/mol]
1.0
0.8
0.6
0.4
δ18O [‰, V-PDB]
-3.0
-2.5
-2.0
δ13C [‰, V-PDB]
3.0
2.5
2.0
1.5
Sr/Ca [mmol/mol]
2.8
2.4
2.0
Ba/Ca [µmol/mol]
1.5
1.0
2
4
6
8
10
12
14
16
Distance from inner shell edge [mm]

In contrast to $\delta^{18}O$, the Mg/Ca and Sr/Ca ratio in biogenic carbonates are predominantly paleotemperature proxies only, reflecting paleo-SST independent of salinity, and therefore used to deconvolve the SSS from the SST component of the $\delta^{18}O$ record in biogenic carbonates (e.g., McCulloch et al. 1994; Klein et al. 1996; Watanabe et al. 2001; Lear et al. 2002; Ren et al. 2002). The good qualitative agreement of Mg/Ca with the stable oxygen isotope records of LGS1 (Fig. 9) suggests that $\delta^{18}O_{shell}$ mainly reflects SST.

Interpreted as such, light $\delta^{18}O$ values reflect warm SSTs (warm seasons) and heavy $\delta^{18}O$ values cold SSTs (cold seasons), respectively. Eight dark-light couples can be assigned to eight $\delta^{18}O$ minima and maxima in both shells and are interpreted as annual couples (Figs. 9, 10). However, smaller-scale variations in the stable isotope profile exist (especially for shell parts formed during adulthood) and can be aligned with respective scale sub-growth bands. Superimposed on a yearly temperature cycle, minor variations in temperature might occur related to complex and varied monsoon systems, variations in the position of the Intertropical Convergence Zone (ITCZ) and/or multiscale variability of the proto-warm pool in the western equatorial Pacific, which could have caused small scale variations in the $\delta^{18}O$ profile and the banding pattern. However, we cannot entirely exclude that these variations are annual in nature as well, in which case the observed (minimal) lifespan of the specimens is longer. Because pristine aragonite has been replaced (by calcite or altered aragonite) at the inner- and outermost shell edges in both shells, the observed eight years must be interpreted as a minimum estimate of the true lifespan.

Mg/Ca correlates well with the $\delta^{18}O$ variations in LGS1 (Fig. 9). Relatively high Mg/Ca ratios correspond to relatively light $\delta^{18}O$ signals and, like the $\delta^{18}O$ record, can be aligned with the darker growth bands within the shell-banding pattern (Fig. 9). This inverse correlation between the Mg/Ca and $\delta^{18}O$ record together with the positive correlation of Mg/Ca in biogenic carbonates with temperature (e.g., Batenburg et al. 2011; Welsh et al. 2011; Quinn and Sampson 2002) suggests that low density dark bands were formed during warm seasons (reflecting warm SSTs), while high density light bands were secreted during cold seasons (reflecting cold SSTs), respectively. This is in agreement with results from other studies on *Tridacna* shells (e.g., Aharon 1991; Watanabe et al. 2004; Batenburg et al. 2011; Welsh et al. 2011). However, there is apparently no universal mechanism in band formation of marine bivalves. Aubert et al. (2009) showed that dark bands in shells of the modern tridacnine *Hippopus hippopus* were secreted during winter periods. Studies on the clam *Mercenaria mercenaria* even indicate significant latitudinal variation regarding growth band formation (Jones and Quitmyer 1996). Modern shells from the northeastern coast of the United States typically form dark bands during the winter season, whereas in the lower latitudes (U.S. south east coast) these form during summer to early fall (Jones and Quitmyer 1996). Moreover, $\delta^{18}O$ records from a Pliocene *Mercenaria campechiensis* from the northeast U.S. show that dark bands correlate with the warmest temperatures of the annual cycle, revealing an opposite pattern to that seen in modern *Mercenaria mercenaria* shells from the same area (Jones and Quitmyer 1996).

The overall gradual rise of Mg/Ca and the increase in amplitude of the oscillations with age of LGS1 (Fig. 9) indicate that Mg/Ca partitioning in the *Tridacna* shells seems to be influenced not only by temperature but also physiologically via the growth rate. Such an ontogenetic trend in Mg/Ca has been reported for modern *Tridacna* shells (Romanek and Grossman 1989; Elliot et al. 2009). Without correction for this ontogenetic trend, quantitative temperature estimates using Mg/Ca are problematic. Nevertheless, the Mg/Ca variations can be utilized to identify seasonal cycles, which is demonstrated by the good inverse correlation between Mg/Ca and $\delta^{18}O$, which exists throughout the whole length of the profiles (Fig. 9). The $\delta^{18}O$ oscillation amplitude changes with shell growth rate changes, similar as seen in the Mg/Ca ratio variability. Shell parts secreted during adulthood are characterized by high amplitude/low frequency variability, while those formed during juvenile stage show low amplitude/high frequency variations. The changes in amplitude are relatively small and we cannot exclude that these are due to environmental changes rather than a biological control. However, similar findings for modern *Tridacna maxima* from the Samoan Islands have been reported (Romanek and Grossman 1989).

Three broad, low amplitude/high frequency oscillations in specimen LGS1 (Fig. 9) can be assigned (given the above above-mentioned interpretation) to three years in the lifetime of the juvenile *Tridacna.* Contrary to the pattern seen in LGS1, an ontogenetic trend of the $\delta^{18}O$ record related to changes in growth rate was not seen in BW4B, which conforms to visual observations of the banding pattern in this individual. No clear correlation between Mg/Ca and the stable oxygen isotope record of BW4B was found (Fig. 10). It is not clear why the Mg/Ca and $\delta^{18}O$ records agree well in case of LGS1, while this does not apply for the corresponding records of BW4B. Species-specific effects, which partly control biomineralization and thus the incorporation of environmental signals into the shell structure, should be considered. Visual examination reveals a weak correlation between Sr/Ca and $\delta^{18}O$. The two records are inversely correlated (light $\delta^{18}O$ agree with high Sr/Ca ratios), which implies that high Sr/Ca ratios reflect warmer seawater temperatures. However, Sr/Ca in modern *Tridacna gigas* specimen from the South China Sea has been reported to be negatively correlated with temperature, implying a positive correlation between $\delta^{18}O$ and Sr/Ca (Yan et al. 2013). Another study demonstrated the ability of Sr/Ca to reflect the daily light cycle and reported negative correlation between Sr/Ca and temperature on a yearly basis (Sano et al. 2012), contrary to our observations.

Temperature Seasonality Estimates

Calculations of SSTs based on the $\delta^{18}O$ data were performed using the commonly accepted aragonitic oxygen isotope temperature equation by Grossman and Ku (1986), $T\ ^{\circ}C = 21.8 - 4.69\ (\delta^{18}O_{shell} - \delta^{18}O_{sw})$, where $\delta^{18}O_{shell}$ is the measured oxygen isotope composition of the (mollusk) shell, and $\delta^{18}O_{sw}$ the oxygen isotope composition of ambient seawater. Usage of this empirical equation enables the conversion of the measured $\delta^{18}O$ values ($\delta^{18}O_{shell}$) into absolute paleotemperatures. However, the stable oxygen isotope composition of the ambient seawater ($\delta^{18}O_{sw}$) at the time of shell formation of the two *Tridacna* shells can only be estimated. We used a $\delta^{18}O_{sw}$ of −0.88‰, similar to Batenburg et al. (2011) for a late–middle Miocene *Tridacna gigas.* Assuming a $\delta^{18}O_{sw}$ for an ice-free greenhouse world of −1.2‰ (Lear et al. 2000) or −1.0‰ (Zachos 1994), and a modern $\delta^{18}O_{sw}$ of −0.28‰ (Lear et al. 2000) for today's icehouse conditions, this value can be considered as a reasonable estimate for the late Miocene climate, characterized by a reestablished major Antarctic ice cover and gradual onset of the Northern Hemisphere glaciation.

The $\delta^{18}O_{shell}$ maxima, minima, and averaged values and the respective calculated paleotemperature data of LGS1 and BW4B are presented in

←

FIG. 10.—Polished thick section of BW4B used for stable isotope analysis, with respective stable isotope and LA-ICPMS profiles. Micromilled section and position of laser track are marked by arrows. Milled sample 1 was recovered from innermost shell edge, while sample 77 was obtained from outermost shell edge. Smoothing of LA-ICPMS data was performed using the moving average.

Table 3. For comparison, we added the $\delta^{18}O$ data of the late to middle Miocene *Tridacna gigas* published in Batenburg et al. (2011) and the respective (calculated) paleotemperatures/paleoseasonality. Using the equation by Grossman and Ku (1986) and assuming $\delta^{18}O_{sw} = -0.88‰$ results in average temperatures of 27.8 °C for LGS1 and 28.5 °C for BW4B (Table 3); using $\delta^{18}O_{sw}$ of −1.2‰, −1.0‰, or −0.5‰ instead of −0.88‰ shifts the absolute paleotemperatures by −1.2, −0.6, or +1.8 °C. The measurement uncertainty produces errors of ±0.2 °C. Our results are very similar to the average temperature of 28.5 °C calculated for the *Tridacna gigas* dataset (Table 3). The good agreement between stable oxygen isotope data of our *Tridacna* shells with those obtained by another independent study confirms our findings toward a well-preserved aragonite microstructure that contains the original geochemical signature. The present day SST yearly average in the Makassar Strait is about 28.5 to 29.5 °C (Chen et al. 2005; Tangdong et al. 2005) and therefore only slightly higher than the estimated temperatures from the Miocene $\delta^{18}O$ records.

The modern Indo-Pacific Warm Pool (IPWP), which influences tropical Pacific climate and ocean circulations and which determines the SST in the Makassar Strait today, did not appear until about 4 Ma (Li et al. 2006). However, a proto–warm pool existed in the western equatorial Pacific (WEP) from the early late Miocene onward (Li et al. 2006; Nathan and Leckie 2009). It is possible that the slight difference between the modern and estimated Miocene SST conditions (apart from uncertain $\delta^{18}O_{sw}$) is due to these different warm pool regimes. Mg/Ca paleotemperature estimates using late Miocene foraminiferan tests from the WEP generated temperatures ranging from 27.3 to 28.2 °C (Nathan and Leckie 2009). The authors suggest that late Miocene surface waters were slightly cooler and more saline than today. Owing to the uncertain $\delta^{18}O_{sw}$ values, these quantitative paleotemperature reconstructions have a built-in error and therefore a more achievable objective is to calculate average temperature seasonality. Assuming eight years of growth and a constant $\delta^{18}O_{sw}$ and using the $\delta^{18}O$ maximum and minimum for each of the eight years, an average seasonality of 4.6 ± 1.7 °C (2 SD) and 2.7 ± 2.1 °C (2 SD) for LGS1 and BW4B has been calculated for the late Miocene. For comparison, we also assessed the seasonality of the Miocene *Tridacna gigas* dataset by Batenburg et al. (2011), which gives an estimated seasonality of 2.1 ± 2.7 °C (2 SD). Even though the *Tridacna gigas* data overall show higher SST fluctuations, the calculated average seasonality is slightly lower, compared to the data of the two presented *Tridacna* shells. The high standard deviation might reflect high and low ENSO periods within the 15 years of growth of this specimen. Overall, the reported variations of all three $\delta^{18}O$ profiles consistently exceed modern seasonal variability in the Makassar Strait, which is <1.5 °C (Tangdong et al. 2005).

It is not possible to decipher the causes of these relatively high seasonality estimates at the current state of knowledge. Several regional factors possibly influenced late Miocene seasonal variability, such as the East Asian monsoon system, seasonal shifts in ocean currents, changes in the upwelling regime, or the incipient restriction of the Indonesian Seaway from late Miocene onward with the development of the WEP proto–warm pool and possible onset of ENSO-type climate variability (Batenburg et al. 2011). Furthermore, local $\delta^{18}O_{sw}$ modifications due to fluvial runoff, upwelling, or evaporation/precipitation processes must be considered. The good qualitative agreement between the Mg/Ca and the stable oxygen isotope profiles in case of LGS1 suggests that $\delta^{18}O_{shell}$ mainly mirrors SST. The occurrence of the *Tridacna* shells within a rich and diverse fossil coral assemblage and the absence of characteristic peaks in the Ba/Ca profiles possibly indicate relatively constant SSS conditions during shell formation and thus seawater uninfluenced by major (variations in) upwelling and/or riverine runoff.

Few model simulations exist that could potentially help in predicting late Miocene seasonality. Galoetti et al. (2010) suggested evidence for Pacific ENSO-type interannual variability during the late Miocene, which is, owing to strong Pacific-Mediterranean teleconnections during this time interval, recorded in varved evaporitic successions from the Mediterranean. According to Huber and Caballero (2003), the Eocene "hothouse" climate experienced Pacific ENSO variability, even greater in amplitude than today. Their modeled predictions are confirmed by recorded ENSO timescale variability in varved sediments from lakes situated within teleconnected regions. Paleoclimate reconstructions using fossil *Nummulites* from Java indicate an annual seasonal temperature shift of 5–6 °C for the middle Eocene, which indicates ~2 °C greater than modern seasonality at this locality (Evans et al. 2013).

CONCLUSIONS

The interiors of both Miocene *Tridacna* shells discussed herein are to a large extent excellently preserved, which could not be expected from their external appearance. Besides well-preserved pristine aragonite, altered aragonitic and calcitic domains were identified. The latter two deviate strongly in their trace elemental composition from pristine aragonite zones. We demonstrate that element/Ca ratios obtained from diagenetically altered zones should not be used as paleoproxies for reconstructions of primary paleoenvironmental conditions during the time of shell formation. Combined usage of XRD, SEM/CL imaging, and LA-ICPMS trace elemental screening has proven effective at detecting diagenetic shell alteration. The good agreement between stable oxygen isotope data and trace elemental records and the overall good alignment with visible growth bands provides evidence for an intact late Miocene geochemical inventory within pristine shell aragonite.

Based on the $\delta^{18}O$ time-series records, average SST paleotemperatures ranging from 27.8 to 28.5 °C were obtained (for $\delta^{18}O_{sw} = -0.88‰$), which indicates slightly cooler late Miocene SST conditions in the Makassar Strait compared with present day. Assuming a lifespan of eight years, the shells reflect a seasonal SST variability of 2.7 ± 2.1 to 4.6 ± 1.7 °C, which exceeds modern-day seasonality in the Makassar Strait two- to threefold.

Despite presenting less than decade-long continuous paleorecords, analysis of these shells contributes to the scarce, seasonally resolved, contiguous tropical SST record for the Miocene. Our reconstructed Miocene SST seasonality provides key input parameters for climate models and allows better assessment of the dynamics of the Miocene tropics. To extend existing records and to ensure that seasonal and subdecadal climate variability is recognized, new and longer records, possibly even from visually altered specimen, are required.

ACKNOWLEDGMENTS

Special thanks to all Throughflow members for help with fieldwork and discussions, Norman Oxtoby for help with CL-imaging, and to Alex Ball and Tomasz Goral (Science Facilities, NHMUK) for help with SEM work. Thanks are extended to the following people at RHUL: Dave Alderton (XRD), Dave Lowry, Nathalie Grassineau and Dave Mattey (stable isotope analysis), Matthew Thirlwall and Christina Manning (TIMS analysis), and Neil Holloway (thin sections). The authors want to thank Sietske Batenburg and an anonymous reviewer for their detailed and constructive reviews, which significantly helped to improve this manuscript, as well as associate editor Ken Johnson for review supervision and helpful comments. This study was conducted under research license 0266/SIP/FRP/XI/2010 issued by RISTEK (Kementerian Riset Dan Teknologi Republik Indonesia) with special thanks to Professor F. Hasibuan and the team of the Indonesian Badan Geologi–Pusat Survei Geologi. As part of the Throughflow Initial Training Network, this work was funded by the Marie Curie Actions Plan, Seventh Framework Program of the European Union (grant no. 237922).

SUPPLEMENTAL MATERIAL

Data is available from the PALAIOS Data Archive: http://www.sepm.org/pages.aspx?pageid=332.

REFERENCES

Aharon, P., 1991, Recorders of reef environment histories: stable isotopes in corals, giant clams and calcareous algae: Coral Reefs, v. 10, p. 71–90.

Aharon, P., and Chappell, J., 1986, Oxygen isotopes, sea-level changes and the temperature history of a coral-reef environment in New Guinea over the last 105 years: Palaeogeography, Palaeoclimatology, Palaeoecology, v. 56, p. 337–379.

Alibert, C., and McCulloch, M.T., 1997, Strontium/calcium ratios in modern *Porites* corals from the Great Barrier Reef as a proxy for sea surface temperature: Calibration of the thermometer and monitoring of ENSO: Paleoceanography, v. 12, p. 345–363.

Allison, N., Finch, A.A., Webster, J.M., and Clague, D.A., 2007, Palaeoenvironmental records from fossil corals: the effects of submarine diagenesis on temperature and climate estimates: Geochimica et Cosmochimica Acta, v. 71, p. 4693–4703.

Aubert, A., Lazareth, C.E., Cabioch, G., Boucher, H., Yamada, T., Iryu, Y., and Farman, R., 2009, The tropical giant clam *Hippopus hippopus* shell, a new archive of environmental conditions as revealed by sclerochronological and $\delta^{18}O$ profiles: Coral Reefs, v. 28, p. 989–998.

Ayling, B.F., McCulloch, M.T., Gagan, M.K., Stirling, C.H., Andersen, M.B., and Blake, S.G., 2006, Sr/Ca and $\delta^{18}O$ seasonality in a *Porites* coral from the MIS 9 (339–303 ka) interglacial: Earth and Planetary Science Letters, v. 248, p. 462–475.

Barbin, V., Brand, U., Hewitt, R.A., and Ramseyer, K., 1995, Similarity in cephalopod shell biogeochemistry since carboniferous: evidence from cathodoluminescence: Geobios, v. 26, p. 701–710.

Batenburg, S.J., Reichart, G.J., Jilbert, T., Janse, M., Wesselingh, F.P., and Renema, W., 2011, Interannual climate variability in the Miocene: high resolution trace element and stable isotope ratios in giant clams: Palaeogeography, Palaeoclimatology, Palaeoecology, v. 306, p. 75–81.

Beckvar, N., 1981, Cultivation, spawning, and growth of the Giant Clams *Tridacna gigas*, *T. derasa*, and *T. squamosa* in Palau, Caroline Islands: Aquaculture, v. 24, p. 21–30.

Billups, K., and Schrag, D.P., 2003, Application of benthic foraminiferal Mg/Ca ratios to questions of Cenozoic climate change: Earth and Planetary Science Letters, v. 209, p. 181–195.

Birck, J.L., 1986, Precison K-Rb-Sr isotopic analysis: application to Rb-Sr chronology: Chemical Geology, v. 56, p. 73–83.

Brand, U., Jiang, G.Q., Azmy, K., Bishop, J., and Montanez, I.P., 2012, Diagenetic evaluation of a Pennsylvanian carbonate succession (Bird Spring Formation, Arrow Canyon, Nevada, USA), 1: Brachiopod and whole rock comparison: Chemical Geology, v. 308–309, p. 26–39.

Cane, M.A., and Molnar, P., 2001, Closing of the Indonesian seaway as a precursor to east African aridification around 3–4 million years ago: Nature, v. 411, p. 157–162.

Chen, M.T., Huang, C.C., Pflaumann, U., Waelbroeck, C., and Kucera, M., 2005, Estimating glacial western Pacific sea-surface temperature: methodological overview and data compilation of surface sediment planktic foraminifer faunas: Quaternary Science Reviews, v. 24, p. 1049–1062.

Chen, T.R., Yu, K.F., Li, S., Chen, T.G., and Shi, Q., 2011, Anomalous Ba/Ca signals associated with low temperature stresses in *Porites* corals from Daya Bay, northern South China Sea: Journal of Environmental Sciences (China), v. 23, p. 1452–1459.

Corrège, T., Gagan, M.K., Beck, J.W., Burr, G.S., Cabioch, G., and Le Cornec, F., 2004, Interdecadal variation in the extent of South Pacific tropical waters during the Younger Dryas event: Nature, v. 428, p. 927–929.

Crowley, T.J., Short, D.A., Mengel, J.G., and North, G.R., 1986, Role of seasonality in the evolution of climate during the last 100 million years: Science, v. 231, p. 579–584.

Denton, G.H., Alley, R.B., Comer, G.C., and Broecker, W.S., 2005, The role of seasonality in abrupt climate change: Quaternary Science Reviews, v. 24, p. 1159–1182.

Elliot, M., Welsh, K., Chilcott, C., McCulloch, M., Chappell, J., and Ayling, B., 2009, Profiles of trace elements and stable isotopes derived from giant long-lived *Tridacna gigas* bivalves: potential applications in paleoclimate studies: Palaeogeography, Palaeoclimatology, Palaeoecology, v. 280, p. 132–142.

England, M.H., and Huang, F., 2005, On the interannual variability of the Indonesian Throughflow and its linkage with ENSO: Journal of Climate, v. 18, p. 1435–1444.

Evans, D., Müller, W., Oron, S., and Renema, W., 2013, Eocene seasonality and alkaline earth reconstruction using shallow-dwelling large benthic foraminifera: Earth and Planetary Science Letters, v. 381, p. 104–115.

Faylona, M.G.P.G., Lazareth, C.E., Semah, A.M., Caquineau, S., Boucher, H., and Ronquillo, W.P., 2011, Preliminary study on the preservation of giant clam (Tridacnidae) shells from the Balobok Rockshelter archaeological site, South Philippines: Geoarchaeology: An International Journal, v. 26, p. 888–901.

Flower, B.P., and Kennett, J.P., 1994, The middle Miocene climatic transition: East Antarctic ice-sheet development, deep-ocean circulation and global carbon cycling: Palaeogeography, Palaeoclimatology, Palaeoecology, v. 108, p. 537–555.

Fluckiger, J., Knutti, R., White, J.W.C., and Renssen, H., 2008, Modeled seasonality of glacial abrupt climate events: Climate Dynamics, v. 31, p. 633–645.

Foster, L.C., Andersson, C., Høie, H., Allison, N., Finch, A.A., and Johansen, T., 2008, Effects of micromilling on $\delta^{18}O$ in biogenic aragonite: Geochemistry, Geophysics, Geosystems, v. 9, doi: 10.1029/2007GC001911.

Gagan, M.K., Ayliffe, L.K., Beck, J.W., Cole, J.E., Druffel, E.R.M., Dunbar, R.B., and Schrag, D.P., 2000, New views of tropical paleoclimates from corals: Quaternary Science Reviews, v. 19, p. 45–64.

Galoetti, S., von der Heydt, A., Huber, M., Bice, D., Dijkstra, H., Jilbert, T., Lanci, L., and Reichart, G.-J., 2010, Evidence for active El Niño Southern Oscillation variability in the late Miocene greenhouse climate: Geology, v. 38, p. 419–422.

Gillikin, D.P., Dehairs, F., Lorrain, A., Steensmans, D., Baeyens, W., and André, L., 2006, Barium uptake into the shells of the common mussel *(Mytilus edulis)* and the potential for estuarine paleo-chemistry reconstruction: Geochimica et Cosmochimica Acta, v. 70, p. 395–407.

Gillikin, D.P., Lorrain, A., Paulet, Y.M., Andre, L., and Dehairs, F., 2008, Synchronous barium peaks in high-resolution profiles of calcite and aragonite marine bivalve shells: Geo-Marine Letters, v. 28, p. 351–358.

Gomez-Alday, J.J., and Elorza, J., 2003, Diagenesis, regular growth and records of seasonality in inoceramid bivalve shells from mid-Maastrichtian hemipelagic beds of the Bay of Biscay: Geologie En Mijnbouw, v. 82, p. 289–301.

Gotte, T., and Richter, D.K., 2009, Quantitative aspects of Mn-activated cathodoluminescence of natural and synthetic aragonite: Sedimentology, v. 56, p. 483–492.

Griffiths, N., Müller, W., Johnson, K.G., and Aguilera, O.A., 2013, Evaluation of the effect of diagenetic cements on element/Ca ratios in aragonitic early Miocene (~ 16 Ma) Caribbean corals: implications for "deep-time" palaeo-environmental reconstructions: Palaeogeography, Palaeoclimatology, Palaeoecology, v. 369, p. 185–200.

Grossman, E.L., and Ku, T.-L., 1986, Oxygen and carbon isotope fractionation in biogenic aragonite: temperature effects: Chemical Geology, Isotope Geochemistry Section, v. 59, p. 59–74.

Grossman, E.L., Mii, H.S., Zhang, C.L., and Yancey, T.E., 1996, Chemical variation in Pennsylvanian brachiopod shells: diagenetic, taxonomic, microstructural, and seasonal effects: Journal of Sedimentary Research, v. 66, p. 1011–1022.

Grove, C.A., Zinke, J., Scheufen, T., Maina, J. Boer, W., Randriamanantsoa, B., and Brummer G.-J.A., 2012, Spatial linkages between coral proxies of terrestrial runoff across a large embayment in Madagascar: Biogeosciences, v. 9, p. 3063–3081.

Hall, R., Cottam, M.A., and Wilson, M.E.J., 2011, The SE Asian gateway: History and tectonics of the Australia–Asia collision: Geological Society of London, Special Publications, v. 355, p. 1–6.

Harriss, R.C., 1965, Trace element distribution in molluscan skeletal material I. Magnesium, iron, manganese and strontium: Bulletin of Marine Science, v. 15, p. 265–273.

Harzhauser, M., Mandic, O., Piller, W.E., Reuter, M., and Kroh, A., 2008, Tracing back the origin of the Indo-Pacific mollusc fauna: Basal Tridacninae from the Oligocene and Miocene of the Sultanate of Oman: Palaeontology, v. 51, p. 199–213.

Hathorne, E.C., Felis, T., James, R.H., and Thomas, A., 2011, Laser ablation ICP-MS screening of corals for diagenetically affected areas applied to Tahiti corals from the last deglaciation: Geochimica et Cosmochimica Acta, v. 75, p. 1490–1506.

Hendy, E.J., Gagan, M.K., Lough, J.M., McCulloch, M., and Demenocal, P.B., 2007, Impact of skeletal dissolution and secondary aragonite on trace element and isotopic climate proxies in *Porites* corals: Paleoceanography, v. 22, doi: 10.1029/2007PA001462.

Hernavan, U.E., 2012, Taxonomy of Indonesian giant clams (Cardiidae, Tridacninae): Biodiversitas, v. 13, p. 118–123.

Herold, N., Huber, M., Müller, R.D., and Seton, M., 2012, Modeling the Miocene climatic optimum: ocean circulation: Paleoceanography, v. 27, doi: 10.1029/2010PA002041.

Holbourn, A., Kuhnt, W., Schulz, M., Flores, J.A., and Andersen, N., 2007, Orbitally-paced climate evolution during the middle Miocene "Monterey" carbon-isotope excursion: Earth and Planetary Science Letters, v. 261, p. 534–550.

Hönisch, B., Allen, K.A., Russel, A.D., Eggins, S.M., Bijma, J., Spero, H.J., Lea, D.W., and Yu, J., 2011, Planktic foraminifers as recorders of seawater Ba/Ca: Marine Micropaleontology, v. 79, p. 52–57.

Huber, M., and Caballero R., 2003, Eocene El Niño: Evidence for robust tropical dynamics in the "hothouse": Science, v. 299, p. 887–881.

Jochum, K.P., Weis, U., Stoll, B., Kuzmin, D., Yang, Q.C., Raczek, I., Jacob, D.E., Stracke, A., Birbaum, K., Frick, D.A., Gunther, D., and Enzweiler, J., 2011a, Determination of reference values for NIST SRM 610–617 glasses following ISO guidelines: Geostandards and Geoanalytical Research, v. 35, p. 397–429.

Jochum, K.P., Wilson, S.A., Abouchami, W., Amini, M., Chmeleff, J., Eisenhauer, A., Hegner, E., Iaccheri, L.M., Kieffer, B., Krause, J., McDonough, W.F., Mertz-Kraus, R., Raczek, I., Rudnick, R.L., Scholz, D., Steinhoefel, G., Stoll, B., Stracke, A., Tonarini, S., Weis, D., Weis, U., and Woodhead, J.D., 2011b, GSD-1G and MPI-DING reference glasses for *in situ* and bulk isotopic determination: Geostandards and Geoanalytical Research, v. 35, p. 193–226.

Jones, D.S., and Quitmyer, J.R., 1996, Marking time with bivalve shells: oxygen isotopes and season of annual increment formation: PALAIOS, v. 11, p. 340–346.

Jones, D.S., William, D.F., and Romanek, C.S., 1986, Life history of symbiont-bearing giant clams from stable isotope profiles: Science, v. 231, p. 46–48.

Klein, R.T., Lohmann, K.C., and Thayer, C.W., 1996, Bivalve skeletons record sea-surface temperature and $\delta^{18}O$ via Mg/Ca and $^{18}O/^{16}O$ ratios: Geology, v. 24, p. 415–418.

Kuhnt, W., Holbourn, A., Hall, R., Zuvela, M., and Kase, R., 2004, Neogene history of the Indonesian throughflow: Continent-ocean interactions within East Asian marginal seas, v. 149, p. 299–320.

Langlet, D., Alunno-Bruscia, M., Rafelis, M., Renard, M., Roux, M., Schein, E., and Buestel, D., 2006, Experimental and natural cathodoluminescence in the shell of *Crassostrea gigas* from Thau lagoon (France): ecological and environmental implications: Marine Ecology Progress Series, v. 317, p. 143–156.

Lazareth, C.E., Vander Putten, E., André, L., and Dehairs, F., 2003, High-resolution trace element profiles in shells of the mangrove bivalve *Isognomon ephippium*: a record of environmental spatio-temporal variations?: Estuarine, Coastal and Shelf Sciences, v. 57, p. 1103–1114.

Lear, C.H., Elderfield, H., and Wilson, P.A., 2000, Cenozoic deep-sea temperatures and global ice volumes from Mg/Ca in benthic foraminiferal calcite: Science, v. 287, p. 269–272.

Lear, C.H., Rosenthal, Y., and Slowey, N., 2002, Benthic foraminiferal Mg/Ca-paleothermometry: a revised core-top calibration: Geochimica et Cosmochimica Acta, v. 66, p. 3375–3387.

Li, Q., Li, B., Zhong, G., McGowran, B., Zhou, Z., Wang, J., and Wang, P., 2006, Late Miocene development of the western Pacific warm pool: planktonic foraminifer and oxygen isotopic evidence: Palaeogeography, Palaeoclimatology, Palaeoecology, v. 237, p. 465–482.

Longerich, H.P., Gunther, D., and Jackson, S.E., 1996, Elemental fractionation in laser ablation inductively coupled plasma mass spectrometry: Fresenius Journal of Analytical Chemistry, v. 355, p. 538–542.

Mayfield, A., and Gates, R., 2007, Osmoregulation in anthozoan-dinoflagellate symbiosis: Comparative Biochemistry and Physiology A, 147, 1–10.

McArthur, J.M., and Howarth, R.J., 2004, Strontium isotope stratigraphy, *in* Gradstein, F.M., Ogg, J.G., and Smith, A.G., eds., A Geological Timescale 2004: Cambridge University Press, Cambridge, U.K., p. 589.

McArthur, J.M., Howarth, R.J., and Bailey, T.R., 2001, Strontium isotope stratigraphy: LOWESS version 3: Best fit to the marine Sr-isotope curve for 0–509 Ma and accompanying look-up table for deriving numerical age: Journal of Geology, v. 109, p. 155–170.

Mcculloch, M.T., Gagan, M.K., Mortimer, G.E., Chivas, A.R., and Isdale, P.J., 1994, A high-resolution Sr/Ca and $\delta^{18}O$ coral record from the Great Barrier Reef, Australia, and the 1982–1983 El Nino: Geochimica et Cosmochimica Acta, v. 58, p. 2747–2754.

Mcculloch, M.T., Fallon, S., Wyndham, T., Hendy, E., Lough, J., and Barnes, D., 2003, Coral record of increased sediment flux to the inner Great Barrier Reef since European settlement: Nature, v. 421, p., 727–730.

McGregor, H.V., and Gagan, M.K., 2003, Diagenesis and geochemistry of *Porites* corals from Papua New Guinea: implications for paleoclimate reconstruction: Geochimica et Cosmochimica Acta, v. 67, p. 2147–2156.

Mertz-Kraus, R., Brachert, T.C., Jochum, K.P., Reuter, M., and Stoll, B., 2009, LA-ICP-MS analyses on coral growth increments reveal heavy winter rain in the Eastern Mediterranean at 9 Ma: Palaeogeography, Palaeoclimatology, Palaeoecology, v. 273, p. 25–40.

Mishima, M., Kawahata, H., Suzuki, A., Inoue, M., Okai, T., and Omura, A., 2009, Reconstruction of the East China Sea palaeoenvironment at 16 ka by comparison of fossil and modern *Faviidae* corals from the Ryukyus, southwestern Japan: Journal of Quaternary Science, v. 24, p. 928–936.

Moberg, F., Nystrom, M., Kautsky, N., Tedengren, M., and Jarayabhand, P., 1997, Effects of reduced salinity on the rates of photosynthesis and respiration in the hermatypic corals *Porites lutea* and *Pocillopora damicornis*: Marine Ecology Progress Series, v. 157, p. 53–59.

Moir, B.G., 1990, Comparative studies of "fresh" and "aged" *Tridacna-gigas* shell: Preliminary investigations of a reported technique for pretreatment of tool material: Journal of Archaeological Science, v. 17, p. 329–345.

Müller, W., Shelley, M., Miller, P., and Broude, S., 2009, Initial performance metrics of a new custom-designed ArF excimer LA-ICPMS system coupled to a two-volume laser-ablation cell: Journal of Analytical Atomic Spectrometry, v. 24, p. 209–214.

Nathan, S.A., and Leckie, R.M., 2009, Early history of the Western Pacific Warm Pool during the middle to late Miocene (~ 13.2–5.8 Ma): role of sea-level change and implications for equatorial circulation: Palaeogeography, Palaeoclimatology, Palaeoecology, v. 274, p. 140–159.

Nothdurft, L.D., and Webb, G.E., 2009, Earliest diagenesis in scleractinian coral skeletons: implications for palaeoclimate-sensitive geochemical archives: Facies, v. 55, p. 161–201.

Pearson, P.N., Ditchfield, P. W., Singano, J., Harcourt-Brown, K.G., Nicholas, C.J., Olsson, R.K., Shackleton, N.J., and Hall, M.A., 2001, Warm tropical sea surface temperatures in the Late Cretaceous and Eocene epochs: Nature, v. 413, p. 481–487.

Quinn, T.M., and Sampson, D.E., 2002, A multiproxy approach to reconstructing sea surface conditions using coral skeleton geochemistry: Paleoceanography, v. 17, doi: 10.1029/2000PA000528.

Ren, L., Lindley, B.K., Wellington, G.M., Schrag, D.P., and Hoegh-Guildberg, O., 2002, Deconvolving the $\delta^{18}O$ seawater component from subseasonal coral $\delta^{18}O$ and Sr/Ca at Rarotonga in the southwestern subtropical Pacific for the period 1726–1997: Geochimica Et Geocosmica Acta, 67, p. 1609–1621.

Renema, W., Bellwood, D.R., Braga, J.C., Bromfield, K., Hall, R., Johnson, K.G., Lunt, P., Meyer, C.P., McMonagle, L.B., Morley, R.J., O'Dea, A., Todd, J.A., Wesselingh, F.P., Wilson, M.E.J., and Pandolfi, J.M., 2008, Hopping hotspots: Global shifts in marine biodiversity: Science, v. 321, p. 654–657.

Renema, W., Warter, V., Novak, V., Young, Y., Marshall, N., and Hasibuan, F., 2015, Ages of Miocene fossil localities in the Northern Kutai Basin (East Kalimantan, Indonesia): PALAIOS, v. 30, p. 26–39.

Romanek, C.S., and Grossman, E.L., 1989, Stable isotope profiles of *Tridacna maxima* as environmental indicators: PALAIOS, v. 4, p. 402–413.

Sano, Y., Kobayashi, S., Shirai, K., Takahata, N., Matsumoto, K., Watanabe, T., Sowa, K., and Iwai, K., 2012, Past daily light cycle recorded in the strontium/calcium ratios of giant clam shells: Nature Communications, v. 3, doi: 10.1038/NCOMMS1763.

Sayani, H.R., Cobb, K.M., Cohen, A.L., Elliott, W.C., Nurhati, I.S., Dunbar, R.B., Rose, K.A., and Zaunbrecher, L.K., 2011, Effects of diagenesis on paleoclimate reconstructions from modern and young fossil corals: Geochimica et Cosmochimica Acta, v. 75, p. 6361–6373.

Singh, R.K., and Gupta, A.K., 2010, Deep-sea benthic foraminiferal changes in the eastern Indian Ocean (ODP Hole 757B): their links to deep Indonesian (Pacific) flow and high latitude glaciation during the Neogene: Episodes, v. 33, p. 74–82.

Srinivasan, M.S., and Sinha, D.K., 2000, Ocean circulation in the tropical Indo-Pacific during early Pliocene (5.6–4.2 Ma): Paleobiogeographic and isotopic evidence: Proceedings of the Indian Academy of Sciences (Earth and Planetary Sciences), v. 109, p. 315–328.

Swart, P.K., Elderfield, H., and Greaves, M.J., 2002, A high-resolution calibration of Sr/Ca thermometry using the Caribbean coral Montastraea annularis: Geochemistry Geophysics Geosystems, v. 3, doi: 10.1029/2002GC000306.

Tangdong, Q., Du, J., Strachan, J., Meyers, G., and Slingo, J., 2005, Sea surface temperature and its variability in the Indonesian region: Oceanography, v. 18, p. 50–61.

Taylor, J.D., Kennedy, W.J., and Hall, A., 1973, The Shell Structure and Mineralogy of the Bivalvia II, Lucininacea–Clavagellacea, Conclusions: Bulletin of the British Museum (Natural History), Zoology, v. 22, p. 255–294.

Thébault, J., Chauvaud, L., L'Helguen, S., Clavier, J., Barats, A., Jacquet, S., Pechéyran, C., and Amouroux, D., 2009, Barium and molybdenum records in bivalve shells: geochemical proxies for phytoplankton dynamics in coastal environments?: Limnology and Oceanography, v. 54, p. 1002–1014.

Thirlwall, M.F., 1991, Long-term reproducibility of multicollector Sr and Nd isotope ratio analysis: Chemical Geology (Isotope Geochemistry Section), v. 94, p. 85–104.

Watanabe, T., and Oba, T., 1999, Daily reconstruction of water temperature from oxygen isotopic ratios of a modern *Tridacna* shell using a freezing microtome sampling technique: Journal of Geophysical Research, v. 104, p. 20667–20674.

Watanabe, T., Winter, A., and Oba, T., 2001, Seasonal changes in sea surface temperature and salinity during the Little Ice Age in the Caribbean Sea deduced from Mg/Ca and $^{18}O/^{16}O$ ratios in corals: Marine Geology, v. 173, p. 21–35.

Watanabe, T., Suzuki, A., Kawahata, H., Kan, H., and Ogawa, S., 2004, A 60-year isotopic record from a mid-Holocene fossil giant clam (*Tridacna gigas*) in the Ryukyu Islands: physiological and paleoclimatic implications: Palaeogeography, Palaeoclimatology, Palaeoecology, v. 212, p. 343–354.

Welsh, K., Elliot, M., Tudhope, A., Ayling, B., and Chappell, J., 2011, Giant bivalves (*Tridacna gigas*) as recorders of ENSO variability: Earth and Planetary Science Letters, v. 307, p. 266–270.

Wendler, J.E., Wendler, I., Rose, T., and Huber, B.T., 2012, Using cathodoluminescence spectroscopy of Cretaceous calcareous microfossils to distinguish biogenic from early-diagenetic calcite: Microscopy and Microanalysis, v. 18, p. 1313–1321.

Yan, H., Shao, D., Wang, Y., and Sun, L., 2013, Sr/Ca profile of long-lived *Tridacna gigas* bivalves from South China Sea: a new high-resolution SST proxy: Geochimica et Cosmochimica Acta, v. 112, p. 52–65.

Zachos, J.C., 1994, From the greenhouse to the icehouse: a Southern Ocean perspective of Paleogene climate: Oceanus, v. 36, p. 57–61.

Zachos, J.C., Pagani, M., Sloan, L., Thomas, E., and Billups, K., 2001, Trends, rhythms, and aberrations in global climate 65 Ma to present: Science, v. 292, p. 686–93.

Zachos, J.C., Dickens, G.R., and Zeebe, R.E., 2008, An early Cenozoic perspective on greenhouse warming and carbon-cycle dynamics: Nature, v. 451, p. 279–283.

Received 18 June 2013; accepted 25 February 2014.